Doctoral Dissertation

Graphene Oxide Membranes with Tailored Interlayer Nanospace for Novel All-Carbon Electrochemical Devices

March 2016

Chikako Ueda

Graduate School of Science and Technology

KUMAMOTO UNIVERSITY

PREFACE

The rapid development of miniaturized electrochemical devices has increased the demand for compact energy storage. Li-ion batteries (LIBs) generally deliver a high energy density but are limited by their low power density and poor cycling lifetime. In contrast, supercapacitors (SCs) deliver much higher power density and exhibit long cycle stability but suffer from a much lower energy density. Accordingly, a new energy storage device with the combined characteristics of high energy and power densities as well as long cycle life is strongly desired as a solution to bridge the gap between LIBs and SCs. In addition, such energy storage devices should preferably be composed of thin, light-weight, inexpensive, safe, easily acquired materials and be capable of being fabricated through a relatively simple manufacturing process.

Graphene oxide (GO) and reduced GO (rGO) show several key properties that can address emerging energy needs, particularly for the ever growing market of portable and wearable energy conversion and storage devices. GO exhibits excellent properties, including high water permeability, good ion and gas selectivity, and high proton conductivity; these properties arise from the presence of various oxygenated functional groups. Thus, GO can be used as both the separator and electrolyte to simplify the fabrication of the device, because GO is simultaneously a good ionic conductor and an electrical insulator. In comparison, rGO, which exhibits high electrical conductivity and high specific surface area, can be used in various electrodes of electrical devices such as LIBs and SCs. Although most GO-based devices are fabricated either with GO as the electrolyte or with a rGO electrode, a rGO/GO/rGO hybrid structure, which comprises a GO electrolyte/separator and rGO electrodes, is attractive because of the potential to develop an all-carbon energy device. Based on these considerations, the rGO/GO/rGO structure is expected to perform as an electrical device.

This work aims (1) to explore the new functionalities of interlayer nanospace in multilayered GO and (2) to investigate the electrochemical properties of both an all-carbon

supercapacitor (Graphene Oxide Supercapacitor: GOSC) and an all-carbon redox battery (Graphene Oxide Redox Battery: GORB) consisting of rGO/GO/rGO.

This thesis is composed of four chapters.

Chapter 1 narrates the general background, preparation method, properties, and applications of GO and rGO.

Chapter 2 presents new functionalities of the interlayer nanospace in multilayered GO for ion diffusion and reactions at the metal/GO (M/GO) interface. Permeation of metal from the surface into GO paper bulk at the M/GO interface was observed at room temperature for metals such as Cu, Ag, Ni, Au, and Pt. Cu, Ag, and Ni quickly permeated GO as ions into the bulk under humid conditions. At first, these metals changed to hydrated ions as a result of redox reactions (with reduction of GO) at the surface, and then permeated the interlayers. Au and Pt were observed to permeate GO as atoms into the GO bulk at room temperature, although the permeation rates were low. These results were considered to be due to the presence of many defects and/or edges with oxygenated groups in the GO paper.

Chapter 3 presents that development of new all-carbon electrochemical devices—GOSC and GORB. A device with an rGO/GO/rGO structure was fabricated and subsequently observed to function as both a SC and a battery depending on the working voltage. The rGO/GO/rGO device operated as a proton-type SC at working potentials as high as 1.2 V. The charge storage mechanism of GOSC resulted from (1) proton conductivity and (2) polarized/separated water molecules in the interlayer spacing of the nanoscale GO. At potentials greater than 1.5 V, it behaved as a battery that operates on the basis of the redox reactions between the oxygenated functional groups on rGO. We deduced the following two hypotheses for the redox mechanism of the GORB: (1) cathode: C=O + $H^+ + e^- \leftrightarrow$ C–OH; anode: CH (defect) + $CO_2 \leftrightarrow$ 2C=O (or C–O) + $H^+ + e^-$; or (2) cathode: $4H^+ + 4e^- + O_2 \leftrightarrow H_2O$; anode: CH (defect) + $CO_2 \leftrightarrow$ 2C=O (or C–O) + $H^+ + e^-$.

Chapter 4 gives the general conclusion of the thesis. In this work, we demonstrated (1) new functionalities of interlayer nanospace in multilayered GO for ion diffusion and reaction at the M/GO interface. We also succeeded in the synthesis and operation of (2) new all-carbon electrochemical devices—Graphene Oxide Supercapacitor (GOSC) and Graphene Oxide Redox Battery (GORB)—with tunable SC and battery behavior *via* the working voltage for the first time to our knowledge. The redox reaction at the M/GO interface and ion diffusion behavior based on unique interlayer nanospace in the GO membrane must be an important aspect of the development of solid GO electrolytes including metal ions for the electrochemical device. Moreover, we believe that an all-carbon electrochemical device, which functions as both a SC and battery, is attractive and will evolve as a next generation electrochemical device.

CONTENTS

CHAPTER 1

Introduction

1.1. General background

The current trend with portable electronics lies in continuous miniaturization while enhancing the functionality and reliability of existing components.[1] However, the integration of energy-storage units, such as batteries and supercapacitors, with electronic circuits is challenging and often limits the miniaturization of the entire system. This is because the necessary energy-storage components scale down poorly in size.

Graphene, which consists of a one-atom-thick nanosheet comprising a sp^2-bonding carbon structure, is a promising electrode material owing to its high theoretical surface area (SSA) of 2,630 $m^2\ g^{-1}$ and ability to facilitate electron or hole transfer (200,000 $cm^2\ v^{-1}s^{-1}$) along its two-dimensional surface.[2,3] In 2004, Geim and Novosolov showed that thin transparent adhesive tape could be used to exfoliate graphite into single atomic layers of graphene and demonstrated atomically thin devices.[4] Thus, graphene exhibits several key properties that can address emerging energy needs, particularly for the ever growing market of portable and wearable energy conversion and storage devices. Graphene is produced by exfoliation of highly-ordered pyrolytic graphite (HOPG),[5] epitaxial growth,[6] and chemical vapor deposition (CVD).[7] However, it suffers from high cost, low yield, and a production rate that is not technologically scalable in its current form.[8]

One possible solution is the reduction of graphene oxide (GO), which is achieved by exfoliation of graphite oxide.[9] Using this technique, a large amount of reduced graphene oxide (rGO) can be easily produced at a very low cost. Notably, it has been demonstrated that the electrical conductivity of rGO can be restored close to the level of graphene by reduction. Thus, rGO, which exhibits high electrical conductivity and high SSA, can be used in various electrodes of electrical

devices.

GO is not only a precursor for the fabrication of rGO but also one of the most promising materials with excellent properties such as high water permeability, [10] good ion and gas selectivity, [11] high proton conductivity[12] and electronic insulating property. These properties arise from the presence of various oxygenated functional groups. Thus, GO can be used as both the separator and electrolyte to simplify the device fabrication, because GO is simultaneously a good ionic conductor and an electrical insulator. Moreover, the interlayer nanospace in multi-layered GO has very unique properties owing to the presence of two types of layers: (1) π–π hydrophobic interaction layers and (2) hydrophilic interaction layers. Therefore, it is also important to explore new functionalities of the interlayer nanospace in multilayered GO.

Based on these considerations, the rGO/GO/rGO structure, which is composed of a GO electrolyte/separator and rGO electrodes, is expected to perform as an electrical device. In this work, we aimed (1) to explore the new functionalities of the interlayer nanospace in multilayered GO and (2) to investigate the electrochemical properties of both an all-carbon supercapacitor (Graphene Oxide Supercapacitor: GOSC) and an all-carbon redox battery (Graphene Oxide Redox Battery: GORB) consisting of rGO/GO/rGO.

1.2. Materials

Figure 1-1 shows the structure of graphene-based nanosheets, graphene, GO, and rGO. In particular, we studied GO and rGO.

1.2.1. Graphene Oxide (GO)

In general, GO is prepared *via* a two-step solution process as illustrated in Figure 1-2. First, graphite oxide is obtained by the oxidative treatment of graphite *via* one of three principal methods

developed by Hummer and Offeman,[13] Staudenmaier,[14] and Brodie.[15] All three methods involve oxidation of graphite to various levels. The Hummers' method is the most common oxidation method. Second, GO is synthesized by exfoliation of graphite oxide. Because of the increased interlayer space and weakened van der Waals force between adjacent layers caused by the introduction of oxygenated functional groups, graphite oxide can be easily exfoliated into individual GO nanosheets. Physical exfoliation using ultrasonic irradiation and chemical exfoliation using reagents, such as tetrabutylammonium, have been reported as exfoliation methods used to obtain GO from graphite oxide. In these exfoliation methods, ultrasonication of graphite oxide has been extensively used because it is easy, cheap, and nontoxic.

Figure 1-1(b) shows a structure of GO. The GO has an approximate thickness of 1 nm and width of several micrometers. This 2D structure has several advantages such as a high SSA. GO consists of π-conjugated sp^2 domains surrounded by an insulating matrix of the sp^3 domains with oxygenated functional groups. According to the most recent study, GO consists of oxidized graphene sheets having their basal planes decorated mostly with epoxide and hydroxyl groups in addition to carbonyl and carboxyl groups located presumably at the edges.[9,19] The polar oxygen functional groups of GO render it hydrophilic; GO disperses particularly well in water and other polar solvents. GO can produce chemical-modified GO using various chemical reactions that provide either covalent or noncovalent attachment. Moreover, composite materials can be easily produced, thereby combining with positively charged materials using a negatively charged GO surface. Such approaches, which add functionality to groups already present on the GO, render more versatile GO-based materials for a wide range of applications.

A free-standing GO paper can be made by vacuum filtration of individual GO nanosheets.[16] Interlayer nanospace in multilayered GO presents two types of layers: (1) π–π hydrophobic interaction layers based on the graphene domain and (2) hydrophilic interaction layers

derived from the oxygen functional group. In general, organic gas is transferred *via* hydrophobic interaction layers. Water molecules and metal ions are moved *via* hydrophilic interaction layers. Therefore, it is important to explore the new functionalities of the interlayer nanospace in multilayered GO. Furthermore, GO exhibits excellent membrane properties, including electrical insulator,[17] high water permeability,[10] good ion and gas selectivity[11] and high proton conductivity;[12] these properties arise from the presence of various oxygenated functional groups. These advantages have led to the applications of GO as a solid electrolyte for energy storage devices.

1.2.2. reduced Graphene Oxide (rGO)

GO is an electrically insulating material owing to its sp^3 bonding networks. As electrical conductivity can be recovered by restoring the π-network, one of the most important reactions of GO is its reduction.[18] Reduction can be achieved through chemical, thermal, electrochemical, or photoreduction pathways.[19] Chemical reduction of the obtained colloidal dispersions has been performed with several reducing agents such as hydrazine,[9] hydroquinone,[20] sodium borohydride ($NaBH_4$),[21] and ascorbic acid.[22] Reduction *via* thermal treatment has been reported to be an efficient and low cost method, producing thermally-expanded GO material with a Brunauer-Emmett-Teller (BET) surface area of 600–900 $m^2\ g^{-1}$.[23] Electrochemical reduction has been presented as an effective way to remove oxygen functional groups from GO.[24] Reduction began at −0.60 V and reached a maximum at −0.87 V.[19] Another final method that shows promise for the reduction of GO relies on photoreduction to remove all of the oxygen functionalities.[25] In principle, this method could avoid contamination derived from the use of dangerous reductants (*e. g*., hydrazine). It is possible to pattern any GO surfaces into an rGO/GO structure in various geometries.

Figure 1-1 (c) shows a structure of rGO. Although reduction removes most of the oxides, the structure of rGO, a highly defective form, is different from that of pristine graphene. Notably, it

has been demonstrated that the electrical conductivity of rGO can be restored close to the level of graphene by reduction. The electric conductivity of rGO has been measured to be 2400 ± 200 S m^{-1} compared with 2500 ± 20 S m^{-1} for graphite and 0.021 ± 0.002 S m^{-1} for GO.[9] rGO exhibits hydrophobicity owing to a decrease in the polar functionality on the surface of the platelet. In addition, rGO can be modified by noncovalent physisorption of both polymers and small molecules onto their basal planes *via* π–π stacking or van der Waals interactions.

Recently, we demonstrated that GO converts into rGO with different reduction levels as well as successful control of the proton and electron conductivity using a photoreduction method.[26,27] The proton conductivity of rGO decreased when the epoxide content and layer distance decreased, whereas the electron conductivity of rGO drastically increased with decreasing oxygen content. Both the proton and electron conduction mechanisms for GO and rGO were discussed based on the concentrations of various functional groups and defects, changes in the interlayer distance, and the activation energy associated with proton conduction. These results indicate that suitable electrode materials can be obtained to control the reduction level of rGO by using a photoreduction method. For example, the middle reduction level of rGO can be used as pseudo-capacitive electrodes. Therefore, among the various reduction methods, we considered that rGO obtained by photoreduction is the most promising material to use as an electrode in an energy storage device.

1.3. Energy Storage Device using rGO electrodes

A sheet of graphene has a theoretical SSA of 2,630 m^2 g^{-1}. This is much larger than that reported to date for carbon black (typically smaller than 900 m^2 g^{-1})[28] or for carbon nanotubes (CNTs), from ~100 to 1000 m^2 g^{-1},[29] but is similar to activated carbon (carbon processed with oxygen to make it porous).[30] The large SSA of graphene—when combined with its high electrical conductivity,[31] high mechanical strength,[32] ease of functionalization,[33] and potential for mass

production[34]—makes it an ideal platform for energy applications, such as a transparent conductive electrode for solar cells, as catalysts for fuel cells, or as flexible high capacity electrodes in Li-ion batteries (LIBs) and supercapacitors (SCs).[28] In particular, we focus on SCs and LIBs using a rGO electrode in this section.

1.3.1. Supercapacitor

A conventional supercapacitor (SC) consists of two activated carbon electrodes (symmetric or asymmetric) and a separator sandwiched between them that is sealed in organic or aqueous electrolyte liquid (Figures 1–3).[35] In a SC, energy is stored by forming an electrical double layer of electrolyte ions on the surface of conductive electrodes. SCs can deliver much higher power density (5–10 kW kg^{-1}) and exhibit long cycle stability (exceeding 1×10^5 cycles), but suffer from a much lower energy density (less than 10 Wh g^{-1}).[36] The electrode, which has higher and more accessible surface area than that of conventional activated carbon electrodes (SSA: 300–2,200 m^2 g^{-1}, electric conductivity: 300 S cm^{-1}) while maintaining high conductivity, is required to increase the energy density.

Graphene-based materials are attractive in this regard because of their mechanical and electrical properties as well as exceptionally high surface areas. Recently, the intrinsic capacitance of single-layer graphene was reported to be ~21 μF cm^{-2}; this value now sets the upper limit for electrochemical double layer capacitance for all carbon-based materials.[37] Thus, SCs based on graphene materials could, in principle, achieve an electrochemical double layer capacitance as high as ~550 F g^{-1} if their entire surface area could be used.[38] Currently, graphene-based materials derived from GO can be manufactured on the ton-scale at low cost, making them potentially cost-effective materials for charging storage devices. Although these graphene-based materials have shown excellent power density and life-cycle stability, their specific capacitance (130 F g^{-1} in

aqueous potassium hydroxide and 99 F g^{-1} in an organic electrolyte) still falls far below the theoretical value of 550 F g^{-1} calculated for single-layer graphene.[39] A variety of other graphene-based materials derived from GO have also been used, but the values of specific capacitance, energy density, and power density have remained lower than expected—an effect often attributed to the restacking of graphene sheets during its processing as a result of the strong sheet-to-sheet van der Waals interactions. This decrease in the specific surface area of graphene accounts for the overall low capacitance.

1.3.2. Battery

Li-ion batteries (LIBs) consist of an intercalated lithium compound cathode, a graphite anode, and an electrolyte (Figure 1-4). Most of the commercial rechargeable LIBs are based on a $LiCoO_2$ cathode and a graphite anode. This combination has a theoretical energy density of 387 Wh kg^{-1} and a measured energy density of 120 to 150 Wh kg^{-1}, which is higher than that of other batteries such as lead acid (~30 Wh kg^{-1}) and nickel metal hydrides (45 to 68 Wh kg^{-1}).[28] Although LIBs can deliver a high energy density, there are limited by their low power density (less than 1000 W kg^{-1}) and poor cycling lifetime (less than 1000 cycles).

Crucial to the performance of rechargeable batteries is the gravimetric capacity to store Li ions. Compared with graphite, graphene and rGO have a larger theoretical gravimetric capacity. Indeed, graphene-based materials are appealing both as cathodes and anodes.[28] Graphene is used as a substrate for the growth of anode/cathode nanomaterials to achieve higher-rate-performance electrodes with respect to non-conducting materials. However, the power density and cyclability of LIBs are not suitable for large-scale applications compared with SCs. LIBs have unresolved safety issues owing to their flammable organic electrolytes. Moreover, depletion of Li itself is also a challenge.

1.4. All-Carbon Energy Storage Device

A new energy storage device with the combined characteristics of high energy and power densities and long cycle life is strongly desired as a solution to bridge the gap between LIBs and SCs.[40] In addition, such energy storage devices should preferably be composed of thin, light-weight, inexpensive, safe, easily acquired materials and be capable of being fabricated through a relatively simple manufacturing process.

Both GO and rGO show several key properties that can address emerging energy needs. The GO can be used as both the separator and electrolyte, because GO is simultaneously a good ionic conductor and an electrical insulator. The application of GO as a solid electrolyte for SCs[17, 41] and batteries (*e.g.* fuel cells,[42] lead-acid batteries[43] and Li-S batteries[44]) has already been demonstrated. As mentioned above, rGO, which exhibits high electric conductivity and high SSA, can be used in various electrodes of electrical devices such as LIBs, SCs, and hybrid Li-ion capacitors.[28,35,45] Although most GO-based devices are fabricated either with GO as the electrolyte or with an rGO electrode, a rGO/GO/rGO hybrid structure, which comprises the GO electrolyte/separator and rGO electrodes, is attractive because of the potential to develop an all-carbon energy device.

We herein propose a new type of all-graphene-oxide device. An all-carbon rGO/GO/rGO device offers the following advantages over current energy storage devices. First, this device operates without the use of external electrolytes. Hydrated GO is both a good ionic conductor and an electrical insulator, thereby allowing it to function as both an electrolyte and a separator. Second, this device does not contain a binder because of its fully integrated membrane-electrode structure. As a result, the contact resistance at the electrode/electrolyte interface may be reduced. Third, controlling and modifying the oxygenated functional groups on GO may enable the fabrication of different types of batteries that operate *via* various redox reactions. Fourth, the nanoscale interlayer of the GO

membrane, which is a unique reaction field, exhibits excellent properties, including high water permeability, water polarization, and ionic conductivity. As a result, the possibility of fabricating an electronic device that operates on a new mechanism arises. Fifth, stacking the device enables an increase in energy density while maintaining the device's ultrathin construction. Lastly, the fabrication process of an rGO/GO/rGO device, which is only photo irradiation of both surfaces of a GO film, is a simple and inexpensive technique that does not require additional processing or complex operations to produce an energy storage device.

1.5. Objective and Scope of this Thesis

In previous studies, we have studied and developed the following: (1) the mechanism of proton conduction in the GO membrane, (2) rGO fabrication techniques using photo, thermal, and electrochemical reduction methods, and (3) production methods for fuel cells and lead-acid batteries using the GO membrane as the solid electrolyte. By amassing these skills, an all-carbon rGO/GO/rGO electrochemical device is likely to be constructed. In this work, we aimed to explore the new functionalities of the interlayer nanospace in multilayered GO and to investigate the electrochemical properties of both an all-carbon SC (Graphene Oxide Supercapacitor: GOSC) and redox battery (Graphene Oxide Redox Battery: GORB).

The main goals of this study are as follows:

- Investigation of the metal/GO interface with tailored interlayer nanospace.
- Development of new all-carbon electrochemical devices—GOSC and GORB—consisting of an rGO electrode and a GO electrolyte/separator.

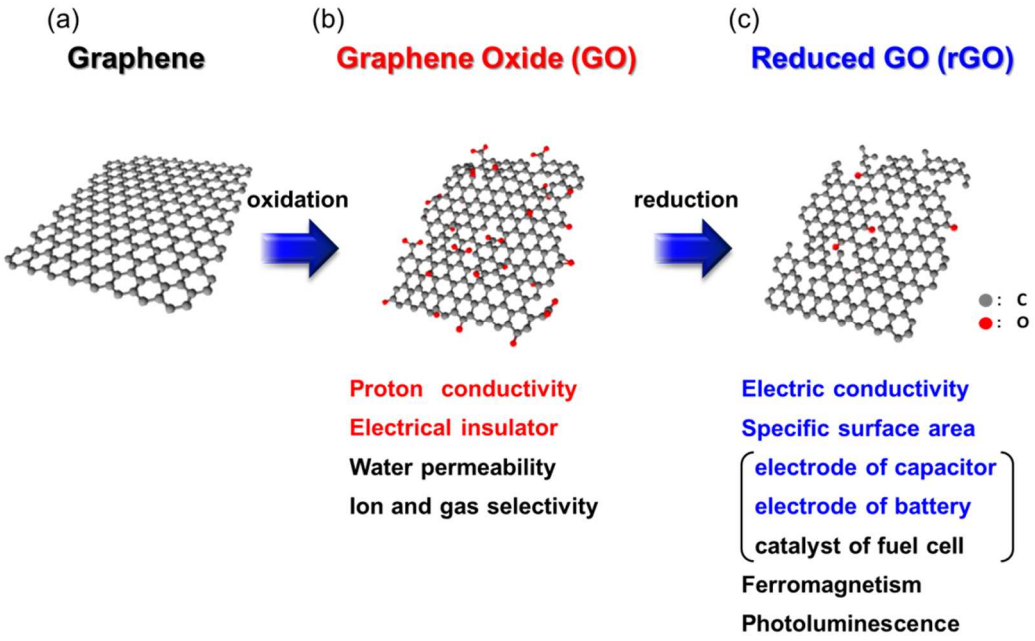

Figure 1-1. Graphene-related materials.

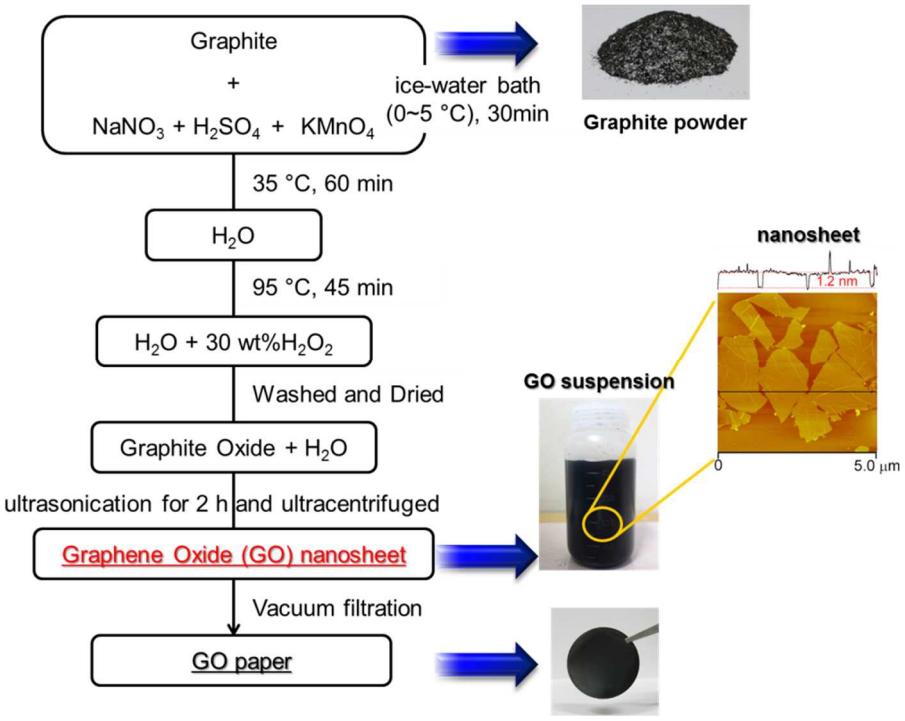

Figure 1-2. Hummers' method for graphene oxide (GO) preparation.

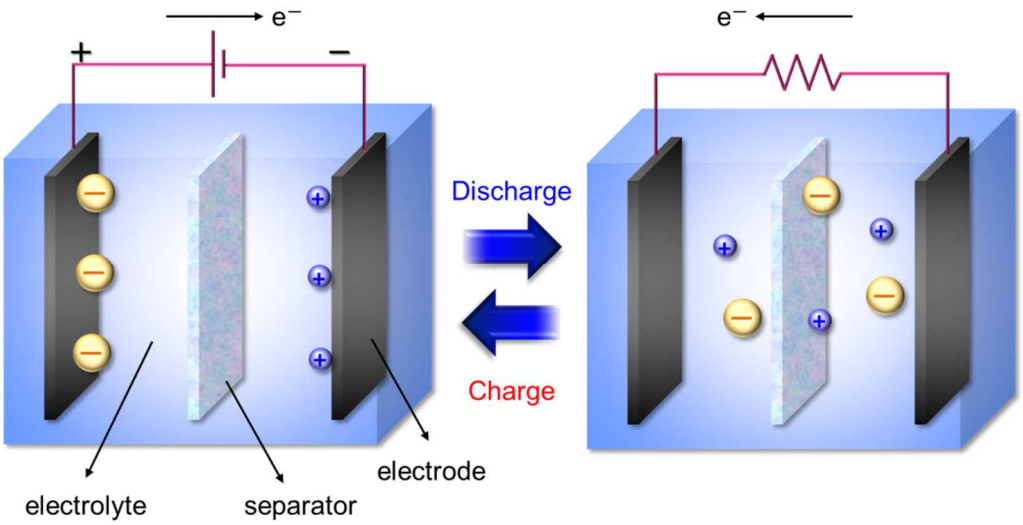

Figure 1-3. Schematic of a supercapacitor.

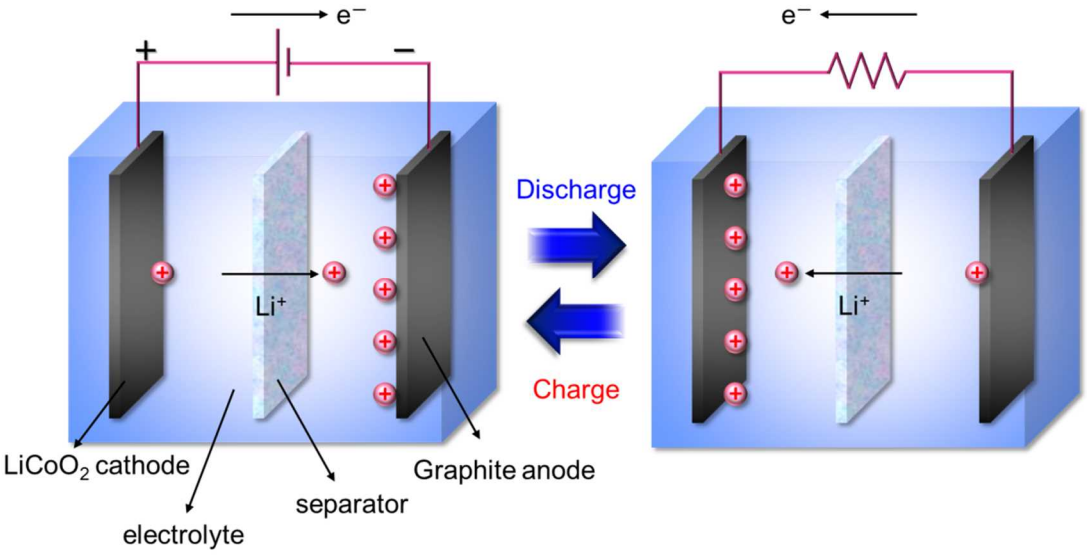

Figure 1-4. Schematic of a Li-ion battery.

References

(1) M. F. El-Kady and R. B. Kaner, *Nat. Commun*., 2013, **4**, 1475.

(2) K. I. Bolotin, K. J. Sikes, Z. Jiang, M. Klima, G. Fudenberg, J. Hone, P. Kim, and H. L. Stormer, *Solid State Commun*. 2008, **146**, 351.

(3) S. V. Morozov, K. S. Novoselov, M. I. Katsnelson, F. Schedin, D. C. Elias, J. A. Jaszczak, and A. K. Geim, *Phys. Rev. Lett*. 2008, **100**, 016602 .

(4) (a)A. K. Geim, *Science*, 2009, 324, 1530-1534; (b) A. K. Geim, and K. S. Novoselov, *Nat. Mater.*, 2007, **6**, 183-191.

(5) K. S. Novoselov, A. K. Geim, S. V. Morozov, D. Jiang, Y. Zhang, S. V. Dubonos, I. V. Grigorieva, and A. A. Firsov, *Science*, 2004, **306**, 666-669.

(6) C. Berger, Z. Song, X. Li, X. Wu, N. Brown, C. Naud, D. Mayou, T. Li, J. Hass, A. N. Marchenkov, E. H. Conrad, P. N. First, and W. A. de Heer, *Science*, 2006, **312**, 1191-1196.

(7) K. S. Kim, Y. Zhao, H. Jang, S. Y. Lee, J. M. Kim, K. S. Kim, J. H. Ahn, P. Kim, J. Y. Choi, and B. H. Hong, *Nature*, 2009, **457**, 706-710.

(8) S. Pei, and H. M. Cheng, *Carbon*, 2012, **50**, 3210-3228.

(9) S. Stankovich, D. A. Dikin, R. D. Piner, K. A. Kohlhaas, A. Kleinhammes, Y. Jia, Y. Wu, S. T. Nguyen, and R. S. Ruoff, *Carbon*, 2007, **45**, 1558-1565.

(10) R. R. Nair, H. A. Wu, P. N. Jayaram, I. V. Grigorieva, and A. K. Geim, *Science*, 2012, **335**, 442-444.

(11) (a) H. W. Kim, H. W. Yoon, S. M. Yoon, B. M. Yoo, B. K. Ahn, Y. H. Cho, H. J. Shin, H. Yang, U. Paik, S. Kwon, J. Y. Choi, and H. B. Park, *Science*, 2013, **342**, 91-95; (b) P. Sun, F. Zheng, M. Zhu, Z. Song, K. Wang, M. Zhong, D. Wu, R. B. Little, Z. Xu, and H. Zhu, *ACS Nano*, 2014, **8**, 850-859.

(12) (a) M. R. Karim, K. Hatakeyama, T. Matsui, H. Takehira, T. Taniguchi, M. Koinuma, Y.

Matsumoto, T. Akutagawa, T. Nakamura, S. Noro, T. Yamada, H. Kitagawa, and S. Hayami, *J. Am. Chem. Soc.*, 2013, **135**, 8097-8100; (b) K. Hatakeyama, M. R. Karim, C. Ogata, H. Tateishi, A. Funatsu, T. Taniguchi, M. Koinuma, S. Hayami, and Y. Matsumoto, *Angew. Chem. Int. Ed.*, 2014, **53**, 6997-7000.

(13) W. S. Hummers, and R. E. Offeman, *J. Am. Chem. Soc.*, 1958, **80**, 1339.

(14) L. Staudenmaier, *Ber. Dtsch. Chem. Ges.*, 1898, **31**, 1481-1487.

(15) B. C. Brodie, *Philos. Trans. R. Soc. Lond.*, 1859, **149**, 249-259.

(16) D. A. Dikin, S. Stankovich, E. J. Zimney, R. D. Piner, G. H. B. Dommett, G. Evmenenko, S. T. Nguyen, and R. S. Ruoff, *Nature*, 2007, **448**, 457-460.

(17) W. Gao, N. Singh, L. Song, Z. Liu, A. L. M. Reddy, L. Ci, R. Vajtai, Q. Zhang, B. Wei, and P. M. Ajayan, *Nat. Nanotechnol.*, 2011, **6**, 496-500.

(18) B. Y. Zhu, S. Murali, W. Cai, X. Li, J. W. Suk, J. R. Potts, and R. S. Ruoff, *Adv. Mater.*, 2010, **22**, 3906-3924.

(19) D. R. Dreyer, S. Park, C. W. Bielawski and R. S. Ruoff, *Chem. Soc. Rev.*, 2010, **39**, 228-240.

(20) G. Wang, J. Yang, J. Park, X. Gou, B. Wang, H. Liu, and J. Yao, *J. Phys. Chem. C*, 2008, **112**, 8192-8195.

(21) Y. Si, and E. T. Samulski, *Nano Lett.*, 2008, **8**, 1679-1682.

(22) V. Dua, S. P. Surwade, S. Ammu, S. R. Agnihotra, S. Jain, K. E. Roberts, S. Park, R. S. Ruoff, and S. K. Manohar, *Angew. Chem. Int. Ed.*, 2010, **49**, 2154-2157.

(23) (a) H. C. Schniepp, J. L. Li, M. J. McAllister, H. Sai, M. Herrera-Alonso, D. H. Adamson, R. K. Prudhomme, R. Car, D. A. Saville, and I. A. Aksay, *J. Phys. Chem. B*, 2006, **110**, 8535-8539; (b) M. J. McAllister, J. L. Li, D. H. Adamson, H. C. Schniepp, A. A. Abdala, J. Liu, M. Herrera-Alonso, D. L. Milius, R. Car, R. K. Prud'homme, and I. A. Aksay, *Chem. Mater.*, 2007, **19**, 4396-4404.

(24) M. Zhou, Y. L. Wang, Y. M. Zhai, J. F. Zhai, W. Ren, F. A. Wang, and S. J. Dong, *Chem. Eur. J.*,

2009, **15**, 6116-6120.

(25) Y. Matsumoto, M. Koinuma, S. Y. Kim, Y. Watanabe, T. Taniguchi, K Hatakeyama, H. Tateishi, and Shintaro Ida, *ACS Appl. Mater. Interfaces*, 2010, **2**, 3461-3466.

(26) K. Hatakeyama, H. Tateishi, T. Taniguchi, M. Koinuma, T. Kida, S. Hayami, H. Yokoi, and Y. Matsumoto, *Chem. Mater*., 2014, **26**, 5598-5604.

(27) K. Hatakeyama, M. S. Islam, M. Koinuma, C. Ogata, T. Taniguchi, A. Funatsu, T. Kida, S. Hayami and Y. Matsumoto, *J. Mater. Chem. A*, 2015, **3**, 20892-20895.

(28) F. Bonaccorso, L. Colombo, G. Yu, M. Stoller, V. Tozzini, A. C. Ferrari, R. S. Ruoff, and V. Pellegrini, *Science*, 2015, **347**, 6217.

(29) A. Peigney, C. Laurent, E. Flahaut, R. R. Bacsa, and A. Rousset, 2001, *Carbon*, **39**, 507-514.

(30) Y. Zhu, S. Murali, M. D. Stoller, K. J. Ganesh, W. Cai, P. J. Ferreira, A. Pirkle, R. M. Wallace, K. A. Cychosz, M. Thommes, D. Su, E. A. Stach, and R. S. Ruoff, 2011, *Science*, **332**, 1537-1541.

(31) A. K. Geim, and K. S. Novoselov, *Nat. Mater.*, 2007, **6**, 183-191.

(32) C. Lee, X. Wei, J. W. Kysar, and J. Hone, *Science*, 2008, **321**, 385-388.

(33) S. Park, and R. S. Ruoff, *Nat. Nanotechnol*., 2009, **4**, 217-224.

(34) F. Bonaccorsoa, A. Lombardoa, T. Hasana, Z. Suna, L. Colombob, and A. C. Ferraria, *Mater. Today*, 2012, **15**, 564-589.

(35) G. Xiong, C. Meng, R. G. Reifenberger, P. P. Irazoqui, and T. S. Fisher, *Electroanalysis*, 2014, **26**, 30-51.

(36) (a)R. Wang, J. Lang, P. Zhang, Z. Lin, and X. Yan, *Adv. Funct. Mater.*, 2015, **25**, 2270-2278; (b) Y. Gogotsi, and P. Simon, *Science*, 2011, **334**, 917-918.

(37) J. Xia, F. Chen, J. Li, and N. Tao, 2009, *Nat. Nanotechnol*., **4**, 505-509.

(38) M. F. El-Kady, V. Strong, S. Dubin, and R. B. Kaner, *Science*, 2012, **335**, 1326-1330.

(39) M. D. Stoller, S. Park, Y. Zhu, J. An, and R. S. Ruoff, *Nano Lett.*, 2008, **8**, 3498-3502.

(40) P. Simon, Y. Gogotsi, and B. Dunn, *Science*, 2014, **343**, 1210-1211.

(41) (a) X. Yang, F. Zhang, L. Zhang, T. Zhang, Y. Huang, and Y. Chen, *Adv. Funct. Mater.*, 2013, **23**, 3353-3360; (b) X. Yang, L. Zhang, F. Zhang, T. Zhang, Y. Huang, and Y. Chen, *Carbon*, 2014, **72**, 381-386.

(42) (a) Ravikumar and K. Scott, *Chem. Commun.*, 2012, **48**, 5584-5586; (b) H. Tateishi, K. Hatakeyama, C. Ogata, K. Gezuhara, J. Kuroda, A. Funatsu, M. Koinuma, T. Taniguchi, S. Hayami, and Y. Matsumoto, *J. Electrochem. Soc.*, 2013, **160**, F1175-F1178.

(43) H. Tateishi, T. Koga, K. Hatakeyama, A. Funatsu, M. Koinuma, T. Taniguchi, and Y. Matsumoto, *ECS Electrochem. Lett.*, 2014, **3**, A19-A21.

(44) J. Q. Huang, T. Z. Zhuang, Q. Zhang, H. J. Peng, C. M. Chen, and F. Wei, *ACS Nano*, 2015, **9**, 3002-3011.

(45) H. Kim, K. Y. Park, J. Hong, and K. Kang, *Sci. Rep.*, 2014, **4**, 5278.

CHAPTER 2

Metal Permeation into Multi-layered Graphene Oxide

Overview

Understanding the chemical and physical properties of metal/graphene oxide (M/GO) interfaces is important when GO is used in electronic and electrochemical devices because the metal layer must be firmly attached to GO. Here, permeation of metal from the surface into GO paper bulk at the M/GO interface was observed at room temperature for metals such as Cu, Ag, Ni, Au, and Pt. Cu, Ag, and Ni quickly permeated GO as ions into the bulk under humid conditions. At first, these metals changed to hydrated ions as a result of redox reactions (with reduction of GO) at the surface, and then permeated the interlayers. Au and Pt were observed to permeate GO as atoms into the GO bulk at room temperature, although the permeation rates were low. These surprising results are considered to be due to the presence of many defects and/or edges with oxygenated groups in the GO paper.

2.1. Introduction

Strong adhesion of metals onto graphene oxide (GO) is highly important for building suitable contacts when GO or reduced GO (rGO) is used in electronic and electrochemical devices. Moreover, the metal/graphene oxide (M/GO) interface itself sometimes acts as a catalytic site for chemical reactions.[1,2] The content of oxygenated functional groups at this interface is expected to be strongly affected by the attachment of metals.[3] Thus, understanding M/GO interfaces at atomic and/or electronic scale may bring about the development of new electronic/spintronic, photochemical, and electrochemical devices because their properties are affected by defects and the content of oxygenated functional groups.[4-6]

The electronic and magnetic properties of transition metals deposited on graphene have been theoretically studied on the basis of *ab initio* density functional theory.[7-12] Au is well-known as a suitable contact material in electronic devices, and has been widely (especially theoretically) studied at Au/graphene or Au/graphite interfaces toward the development of new electronic devices.[13-18] It has been reported that Au atoms attached to graphene nanoribbons move along the edges together with Au–C bonds at high temperature.[16] On the other hand, metal sputtering onto graphene and GO surfaces damages and/or removes the top layer and at the same time changes the GO composition (through reduction).[3] The compositional changes depend on the metal type,[3] suggesting that some reactions occur between the metal and the GO surface.

Here, the unique phenomenon of metal permeation into GO paper bulk (multi-layered GO film) from an M/GO interface is reported. This permeation occurs at room temperature, especially under humid conditions, and two predominant mechanisms of metal ion/atom permeation are suggested.

2.2. Experimental Section

Graphite oxide was prepared by the well-known Hummers' method using 98% graphite powder (Wako Pure Chemical Industries, Ltd.) as the starting material.[19] The GO nanosheet solution (3 g/L) was prepared by exfoliation of GO in pure water by ultrasonication and centrifuged at 10000 rpm to remove any aggregated GO. The GO nanosheet solution was filtered using a membrane filter having a 0.4 μm pore size. The GO paper was obtained by exfoliation from the filter, followed by drying at room temperature under vacuum. The thickness of the GO paper was about 20 μm according to cross-sectional FE-SEM performed using a SU-8000 field-emission SEM (Hitachi High Technologies, Ltd.). Metals (Cu, Ag, Ni, Au, and Pt, The Nilaco Co.) were deposited onto the GO paper surface using a K575X sputter coater (Emitech Ltd.) to a thickness of about 17 nm for

acquiring XPS depth profiles and about 200 nm for performing cross-sectional EPMA, unless otherwise stated. The sputtering time of the samples used for cross-sectional EPMA was set to 10 times that for the samples used for XPS depth profile acquisition. After keeping the M/GO samples under vacuum and under humid conditions at 25 ^{o}C, the following XPS analyses were performed. XPS was carried out using a Sigma Probe XPS analysis system (Thermo Fisher Scientific Inc.), with monochromatic Al-Kα radiation in order to analyze the binding energies and quantitatively analyze the elements in the M/GO samples. The instrument work function was calibrated to give a binding energy of 83.95 eV for an Au4$f_{7/2}$ line for metallic gold, and the spectrometer dispersion was adjusted to give a binding energy of 367.85 eV for metallic Ag3$d_{5/2}$ and 932.65 eV for metallic Cu2$p_{3/2}$. The instrument base pressure was 1×10^{-9} mbar. The depth profiles were obtained by sputtering 3 eV Ar^{+} ions, during which the background pressure in the chamber was 1.0×10^{-7} mbar and a current density of 170 μA cm^{-2} was maintained. Under these conditions, the sputtering rate was approximately 0.2 nm s^{-1} for metal deposited GO films.[20-22] The sputtering rate was set to be substantially lower than the commonly used rate in order to minimize the influence of metal permeation induced by Ar^{+} ion impingement. The reference samples for XPS measurement were copper oxalate hemihydrate ($Cu(COO)_2 \cdot 0.5H_2O$, Wako Pure Chemical Industries, Ltd.) and highly oriented pyrolytic graphite (HOPG, NT-MDT Co., Type-ZYB). The cross sections of the samples were analyzed by means of EPMA (EPMA-1720H, Shimadzu Co., Ltd.) with 5 wavelength-dispersive spectrometers. The experiments were conducted with a focused electron beam current of 5 nA and an acceleration voltage of 15 kV. The samples subjected to cross-sectional EPMA measurements were pulverized in liquid nitrogen and were immediately introduced into the vacuum chamber.

2.3. Results and Discussion

After sputtering of metal atoms onto GO, the GO surface was somewhat reduced due to the high energy of the sputtered metal atoms.[3] The X-ray photoelectron spectroscopy (XPS) spectrum and the cross-sectional field emission scanning electron microscopy (FE-SEM) image of the GO paper without metal deposition are shown in Figure 2-1.[23] Although sputtered metal atoms mainly reduced the epoxy groups of the GO paper, the amount of carbonyl groups hardly changed. Cross-sectional SEM images of the GO paper showed that its thickness was about 20 μm, and GO sheets were piled up in parallel without cracks. Simultaneously, the GO surface composition changed depending on time and the type of metal used (Figure 2-2, 5, 6, 9, 12). The remarkable phenomenon observed here is that permeation of metals occurred from M/GO interface into the GO paper bulk at room temperature at a rate depending on humidity.

Figure 2-2 shows the time dependences of XPS spectra for (a) $Cu2p_{3/2}$ and (b) C1s binding energies and (c) the Cu content at the Cu(17 nm)/GO interface under humid conditions and vacuum at 25 ºC (in Figure 2-2 (b), the XPS spectrum of GO before sputtering is also shown). Note that Cu^{2+} was produced from Cu metal under humid conditions, and that the Cu content at the interface decreased from around 30% to 6% at <30% relative humidity (RH) and to 0% at ≥60% RH (after 24 h, Figure 2-2 (c)). These results imply that Cu changed to Cu^{2+} at the Cu/GO interface (or the GO surface) and then immediately moved into the GO paper bulk under humid conditions. The permeation rate was rather high under high humidity (60% and 90% RH), but low under low humidity. Thus, the presence of vapor is important for fast permeation. According to the XPS analysis of $Cu2p_{3/2}$, Cu^{2+} production was limited under vacuum (Figures 2-2 (a) and 2-3 (a)).

Figure 2-2 (d) shows depth profiles of the Cu content in the region from the Cu/GO interface to the GO paper bulk under 30% RH and vacuum. In all depth profiles presented here,

the GO surface contains a certain amount of Cu because a signal corresponding to Cu is observed at a certain depth even at 0 h. Therefore, the distribution of Cu in depth after a certain time should be evaluated based on comparison with that at 0 h. The decrease of Cu content with time at the surface region (<around 80 nm) suggests fast Cu^{2+} permeation into the bulk. The permeation rate is estimated to be >7 nm/min under 30% RH (>200 nm/30 min, as shown in Figure 2-2 (d)). The low content (<5%) of Cu in the region from the surface to a depth of 200 nm in the present Cu/GO sample after 24 h suggested that all of the coated Cu had permeated deeply into the GO bulk. Furthermore, according to the depth profiles (Figure 2-2 (d)) and the decrease in Cu surface content from around 30% to 21.5% under vacuum (Figure 2-2 (c)), it is possible that Cu also moves as atoms into the GO bulk, although the permeation rate is rather low. The mechanism of the atom diffusion will be similar to those of Au and Pt as described in the later section.

Figure 2-4 shows XPS spectra of $Cu2p_{3/2}$ and C1s of copper(II) oxalate hemihydrate ($Cu(COO)_2 \cdot 0.5H_2O$). According to the C1s spectrum of $Cu(COO)_2$, the peak originating in the carboxyl group of $Cu(COO)_2$ appears near 289.8 eV. Thus, based on Figure 2-2 (b) and Figures 2-3 (a) and (b), the formation of $Cu(COO)_2$ was clear when the peak appeared at 289.8 eV. In particular, under 90% RH, the oxidation of Cu to Cu^{2+} (*i.e.*, production of $Cu(COO)_2$) was remarkably high, as shown in Figure 2-3. Then, the XPS peak intensity decreased with time in the case of 90% RH. These results indicate that Cu^{2+} in $Cu(COO)_2$ produced at the surface permeates the GO paper bulk at the same time H^+ exchange occurs (mainly at COOH groups), especially under high humidity. The permeation rate visibly decreased with increasing the film thickness of Cu, judging from the comparison of the surface content changes in Figure 2-2 (c) (Cu film thickness: 17 nm) and Figure 2-3 (c) (Cu film thickness: 400 nm). No decrease in Cu surface content was observed under vacuum for the thick Cu film (400 nm), as seen in Figure

2-3 (c). These results do not mean that Cu^{2+} ion and Cu atom scarcely diffuse for the case of thick films, because the compositions hardly changes for a large amount of Cu of thick film.

Figure 2-5 shows a mapping of Cu permeating into GO paper, as observed by cross-sectional electron probe microanalysis (EPMA). From cross-sectional EPMA of the as-deposited sample (Figure 2-5 (a)), the thickness of deposited Cu on GO paper was estimated to be about 200 nm. Although this is about 10-fold the thickness of the Cu layer on the sample estimated by XPS depth profile analysis, it is in fact plausible in light of the fact that the sputtering time was 10 times longer for that sample. Cross-sectional SEM images and XRD patterns of GO papers revealed closely packed self-assembled GO sheets. These results suggest that the structure of the GO paper was seldom affected by metal permeation. Cu permeation was clearly observed under humid conditions at 25 ^{o}C (Figures 2-5 (b)-(d)). The distribution of Cu extended from the M/GO interface to a depth of about 6 μm under 30% RH for 1 h (Figure 2-5 (b)). However, when the Cu-deposited sample was kept under 90% RH, in only 10 min, the Cu permeated the GO paper to a remarkable depth extending to the bulk of the GO paper (Figure 2-5 (c)). For the EPMA image of the sample kept under 90% RH for 1 h, the Cu concentration in the GO paper was nearly uniform (Figure 2-5 (d)). These EPMA results suggest that Cu permeation into the GO paper took place rather quickly under high humidity.

The oxidation of Cu led to the reduction of GO under humid conditions, as shown in Figure 2-2 (b), where after 12 h GO began to oxidize due to the termination of Cu^{2+} production. Based on the above results, the following reactions at the surface took place under humid conditions if CH was produced. As a matter of course, other reduction reactions with respect to GO proceed simultaneously.

$$Cu + nH_2O \rightarrow Cu^{2+} + nH_2O + 2e^- \quad (1)$$

$$COx\ (\text{oxygenated groups}) + (2x+1)H^+ + (2x+1)e^- \rightarrow CH + xH_2O \quad (2)$$

Some of the hydrated Cu^{2+} are immediately exchanged with H^+, mainly at COOH sites, to form $Cu(COO)_2$ at the surface, and then move into the interlayers of the GO paper aided by water molecules and H^+ exchange. The permeation model is illustrated in the discussion section.

Figure 2-6 shows (a) the time dependences of the Ag content at the Ag(17 nm)/GO interface and (b) the depth profiles covering the region from the interface to the bulk. Ag permeation occurred much faster under humid conditions than under vacuum, similar to Cu. Although it was difficult to distinguish between Ag and Ag^+ from the binding energy of Ag3d (Figure 2-7), Ag_2O (that is, Ag^+ ion) formation was observed from the XPS spectra of O1s (Figure 2-7). In particular, its formation under vacuum was clear because Ag^+ in Ag_2O hardly moved from the GO surface into the bulk. The O atom in Ag_2O seems to be taken from C-O-C groups because the C-O-C content correspondingly decreased with the formation of Ag_2O, especially under vacuum (Figure 2-7). In any case, the Ag^+/Ag redox reaction, similar to reaction (1) together with reaction (2), occurs at the Ag/GO interface. Consequently, Ag changes to Ag^+ at the interface and then moves into the bulk through the interlayers of the GO paper with the aid of water molecules. The permeation sites are similar to those of H^+, which correspond to bonding sites between C-O-C (and/or OH) groups and water molecules.[5,24,25] According to cross-sectional EPMA mappings of Ag (Figure 2-8), Ag permeated the GO paper at an extremely high rate under 30% RH.

Figure 2-9 shows XPS spectra of (a) $Ni2p_{3/2}$, (b) the time dependences of Ni content at the Ni/GO interface, and (c) depth profiles covering the region from the surface to the bulk. Ni permeation occurred from the Ni/GO interface into the GO bulk, as shown in Figures 2-9 (b) and (c), where the permeation rate increased remarkably under 60% and 90% RH. Oxidation of Ni metal to Ni^{2+} occurred at the surface immediately after sputtering, and then Ni metal disappeared with time following a redox reaction similar to those of Cu and Ag. In fact, GO reduction proceeded with time, as shown in Figure 2-10. Figure 2-11 shows cross-sectional SEM images and EPMA mappings of Ni

and C for the Ni-deposited sample. The layer of Ni remained at the interface under 30% RH for 1 h, which suggests that the permeation rate of Ni into the GO paper was low compared with Cu and Ag. In the case of 90% RH, Ni permeated the GO paper to a sufficient depth, similarly to Cu. These EPMA results were in close agreement with the XPS depth profile data.

Figure 2-12 shows (a) the time dependences of Au and Pt content at the Au/GO and Pt/GO interfaces, respectively, and depth profiles for (b) Au and (c) Pt. Au and Pt were always in the form of elemental metals, as clear from Figure 2-13. Au permeation occurred, although the rate was rather low compared to that of the metal ions examined above, as already stated. The permeation rate for Au atoms increased slightly with increasing the humidity. On the other hand, Pt permeation occurred with relative ease under vacuum, but with difficulty under humid conditions. The depth profiles of Au and Pt are different from each other in terms of metal distribution. Au was smoothly distributed in depth, while the Pt distribution reached maximum at around 30 nm after 3 days. Figure 2-14 shows cross-sectional SEM images and EPMA mappings of Au and C. In the EPMA images of the sample kept for 10 days under 30% RH, slight permeation of Au into the GO paper bulk was observed. However, EPMA could not provide clear evidence of Pt permeation into the GO paper because of the low spatial resolution. According to the XPS depth profile, Au permeated GO from the surface to a depth of around 200 nm, whereas the concentration of Pt in the region from the surface to around 200 nm hardly changed during the experiment. This further confirms that Au and Pt permeate the GO paper bulk as metal atoms at room temperature.

The difference in distribution between Pt and Au may be explained by the M-C bond energy,[26-28] which is higher for Pt-C than for Au-C, leading to relatively smooth permeation for Au. In this regard, the in-plane Au and Pt atom permeation on substrates such as GO and highly oriented pyrolytic graphite (HOPG) at room temperature has been reported.[29-31] Au atom permeation into Si bulk has also been reported to occur even at room temperature with a permeation rate of around 11

nm/10 days (Figure 2-5 in ref. 32).[32] In contrast, the present permeation rate of Au into GO bulk was about 110 nm/7 days (Figure 2-12 (b). This value was estimated from the difference in the sputtering depth at which the Au/(C + Au) = 0.05. Although it is impossible to determine the penetration rate accurately from our EPMA results at the resolution used in the study, Au permeation occurred at a rate of 200 nm/10 days when estimated from the penetration depth of metal, as determined by EPMA (Figure 2-14). These permeation rates of Au into GO bulk are about 10 times faster than in case of Au permeation into Si. Some theoretical studies suggest that defects or edges in graphene act as permeation sites for metal atoms.[14-16,27,28] GO has many defects and edges, both with and without oxygenated functions, which likely act as permeation sites for Au and Pt atoms and result in the permeation of Au and Pt atoms into the GO bulk even at room temperature in the present cases. The effect of water molecules in this phenomenon suggests an important relation of oxygenated functions to the atom permeation mechanism because water molecules interact with these functions, especially in the interlayers.

Two models of the metal permeation mechanism in the M/GO samples are illustrated in Figure 2-15. The first model involves metal ion permeation together with H^+ exchange in the GO interlayers (Figure 2-15 (a)). In this case, the permeation rate is rather high under humid conditions, even at room temperature. This mechanism holds for Cu^{2+}, Ni^{2+}, and Ag^+ permeation in the Cu/GO, Ni/GO, and Ag/GO samples, respectively. In this regard, ion transport through the GO interlayers has been observed for some other ions as well, and the permeation mechanism is similar to that in the present cases.[33,34]

The second mechanism accounts for Au and Pt atom permeation in the Au/GO and Pt/GO samples (Figure 2-15 (b)). It should be noted that Au and Pt atoms move in the GO paper even at room temperature, although the permeation rate is low compared to the cases of metal ions. In these cases, the permeation sites are defects and/or edges, which are abundant in the interlayers of GO

paper. Similar atom diffusion may be occur for Cu, Ag and Ni, because small diffusions were observed in vacuum condition (Figures 2-2 (a) and 2-6 (a)). As shown in Figure 2-16, metal deposited on HOPG, which has neither defects nor edges on the surface, hardly permeated into the bulk. In the case of Au, AuS formation under vacuum was observed in S2p XPS spectra.[35] Figure 2-17 shows time dependences of XPS spectra for S2p under (a) vacuum and (b) 90% RH and (c) S content at the Au/GO interface under vacuum and 90% RH. The amount of AuS increased with increasing time until 7 days under vacuum. The formation of AuS was suggested by trace amounts of SO_4^{2-} present in the GO paper prepared by the Hummers' method (S/C = 0.005). If AuS were generated at the GO surface, internal permeation of Au would be suppressed and the atomization of Au would be inhibited. However, the concentration of S at the surface was almost constant under humid conditions (Figure 2-17 (c)). AuS hardly form under humid conditions (Figure 2-17 (b)) because the SO_4^{2-} ions adsorbed on Au were hydrated. Hydrate formation likely promoted the permeation of Au under humid conditions. In the case of Pt, permeation was faster at the GO surface under vacuum than under humid conditions. Chusuei *et al.* have reported that COO(Pt) or C(=O)COPt forms when Pt nanoparticles are deposited on chemically oxidized carbon nanotubes.[36] Pt atoms will permeate until adsorbing to the carboxyl groups inside GO. Under humid conditions, adsorption of protons to the carboxyl groups that serve as sites for metals to move would inhibit the permeation of Pt. The XPS depth profiles shown in Figure 2-12 (c) also suggest that Pt permeation took place near the GO surface only. As a result, the amount of Pt decreased at the GO surface. Figure 2-18 shows C1s XPS spectra for specimens stored under (a) vacuum and (b) 90% RH for 10 days. When Pt-deposited GO was stored for 10 days under 90% RH, the amount of oxygenated functional groups decreased. This result means that Pt catalyzed reduction of GO under humid conditions.[37] Since the number of sites for Pt permeation decreased when GO was reduced, Pt permeation was suppressed under humid conditions. The details of the permeation mechanisms for

Au and Pt are under investigation for reduced GO paper and GO paper with various added anions.

Furthermore, in order to evaluate the implantation effect caused by impinging Ar^+ ions during XPS depth profiling, permeation of metals such as Cu and Pt in vacuum was investigated after applying Ar^+ ion sputtering for 30 s to the metal-deposited samples (Figure 2-19). Although the surface concentration of metals decreased immediately after Ar^+ ion sputtering, there was almost no further decrease in concentration in the next 24 h. The influence of Ar^+ ion impingement for 30 s was hardly noticeable in the shape of the XPS depth profiles of the samples kept in vacuum for 24 h.

2.4. Conclusion

In conclusion, metal permeation at M/GO interfaces was observed at 25 ^oC, where the metals were deposited onto the surface of GO paper by sputtering. In the cases of M = {Cu, Ag, Ni}, the metals were oxidized to the corresponding ions (Cu^{2+}, Ag^+, and Ni^{2+}) by redox reactions involving the reduction of GO immediately after metal deposition. These ions then quickly permeated through the interlayers into the GO paper bulk. These reactions and fast permeation occurred with ease under humid conditions but with difficulty under vacuum. Au and Pt atoms also permeated the GO paper bulk, although the permeation rates were low. In these cases, abundant defects and/or edges in the GO paper acted as permeation sites. Other metals are also likely to be able to permeate GO paper bulk as atoms. Consequently, GO paper interlayers have unique properties allowing water, metal ions and other atoms to permeate them while providing a shield against gas molecules.[38] These findings are expected to provide important information about GO used in various (especially electrochemical) devices, where ionic movement potentially affects the functionalities.

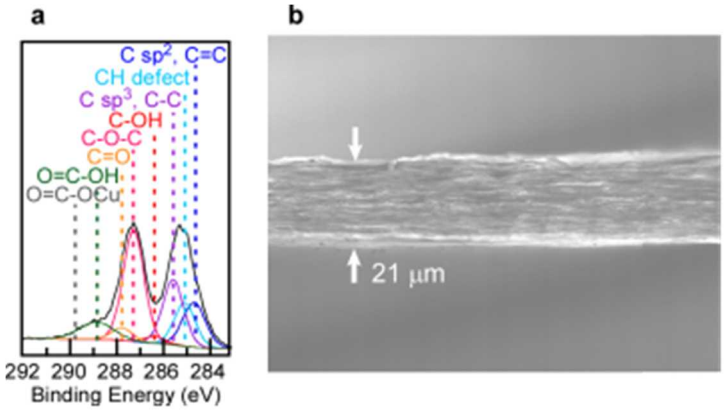

Figure 2-1. (a) XPS spectrum of C1s of the GO paper without metal deposition. (b) Cross-sectional FE-SEM image of GO paper.

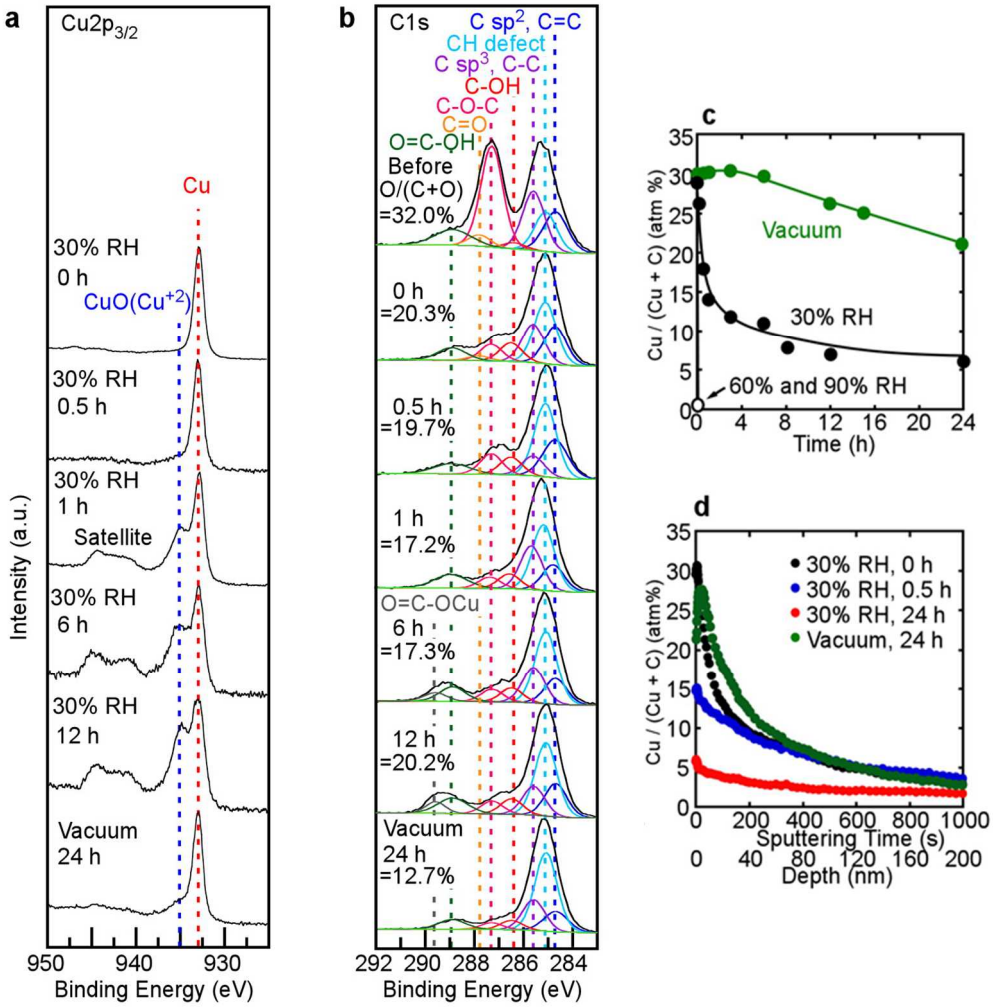

Figure 2-2. Time dependences of XPS spectra, surface content of Cu, and depth profiles of Cu in the Cu(17 nm)/GO sample. (a) Time dependences of XPS spectra of $Cu2p_{3/2}$ at the Cu/GO interface under 30% RH and vacuum. Metallic Cu changed readily to Cu^{2+} (CuO) under 30% RH but hardly did so under vacuum. (b) Time dependences of XPS spectra of C1s at the Cu/GO interface under 30% RH and vacuum. O in O/(C + O) corresponds to the total amount of O in the oxygenated functions of GO. Weak reduction of GO and formation of $Cu(COO)_2$ proceed, but oxidation begins after 12 h. (c) Cu content at the Cu/GO interface as a function of time under humid conditions and vacuum. The Cu content drastically decreased under 60% and 90% RH. (d) Depth profiles of the Cu content at the Cu/GO interface at various times under 30% RH and vacuum. Cu has clearly permeated into the GO bulk.

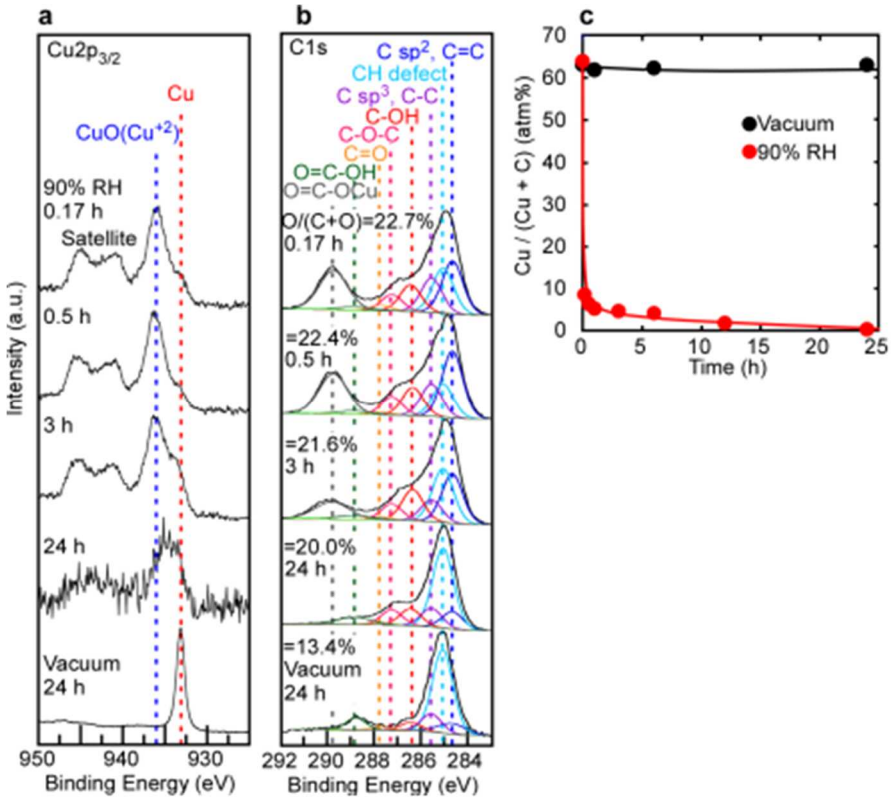

Figure 2-3. Time dependences of XPS spectra and surface content of Cu in the Cu(400 nm)/GO samples under 90% RH and vacuum. (a) Time dependences of XPS spectra of $Cu2p_{3/2}$ at the Cu/GO interface. Metallic Cu changed to Cu^{2+} (CuO) immediately after sputtering under 90% RH but not under vacuum. (b) Time dependences of XPS spectra of C1s at the Cu/GO interface. $Cu(COO)_2$ was produced immediately after sputtering, but its content decreased with time. (c) Cu content at the Cu/GO interface as a function of time under 90% RH and vacuum. The Cu content decreased under 90% RH but not under vacuum.

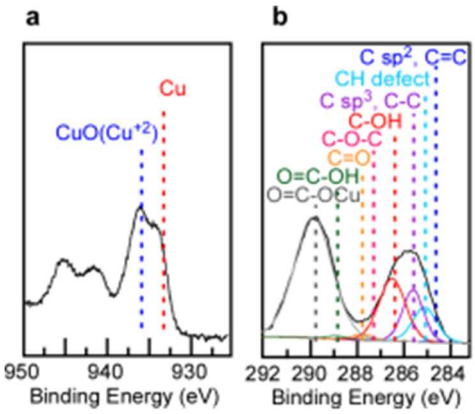

Figure 2-4. XPS spectra of copper(II) oxalate ($Cu(COO)_2$). (a) $Cu2p_{3/2}$ and (b) C1s

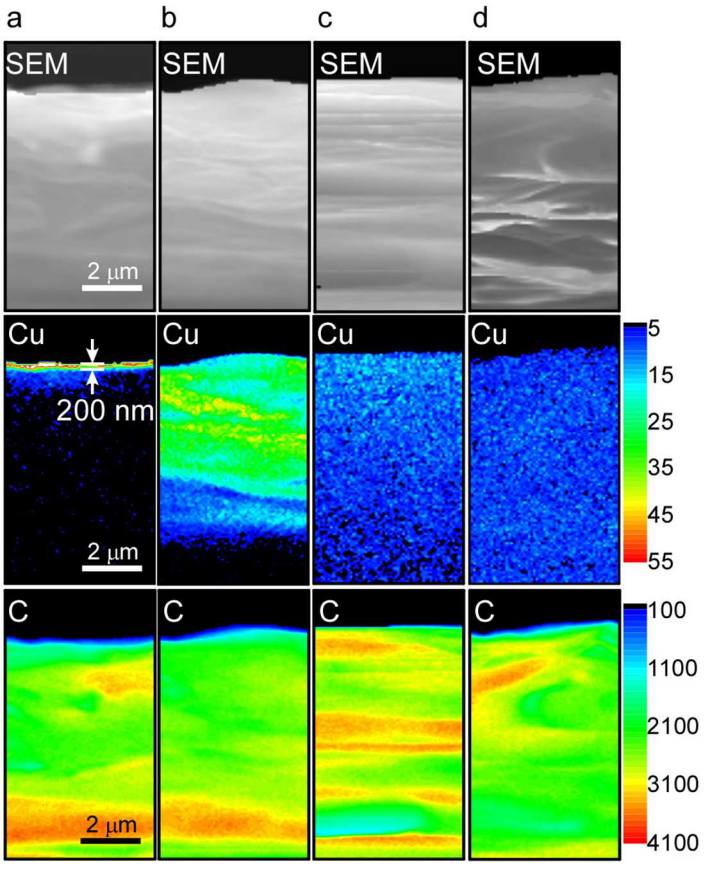

Figure 2-5. Cross-sectional SEM images and EPMA mappings of Cu and C. (a) As-deposited sample, sample kept at (b) 30% RH for 1 h, (c) 90% RH for 10 min, and (d) 90% RH for 1 h. Scale bars denote the concentrations of Cu and C.

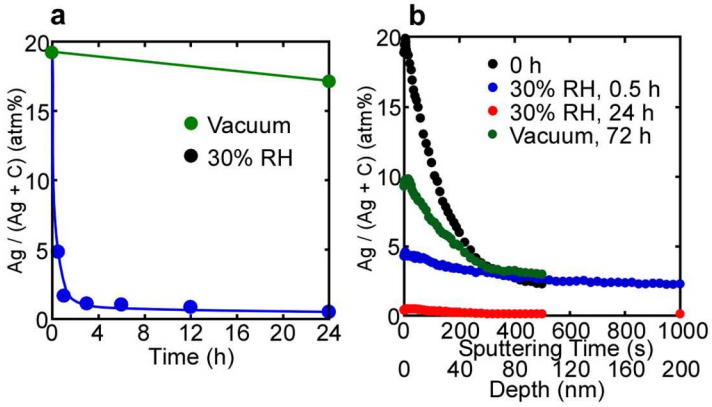

Figure 2-6. Surface content and depth profiles of Ag in the Ag(17 nm)/GO sample. (a) Ag content at the Ag/GO interface as a function of time under 30% RH and vacuum. The Ag content markedly decreased with time under 30% RH, but barely decreased under vacuum. (b) Depth profiles of the Ag content at the Ag/GO interface at various times under 30% RH and vacuum. Ag has clearly permeated the GO bulk.

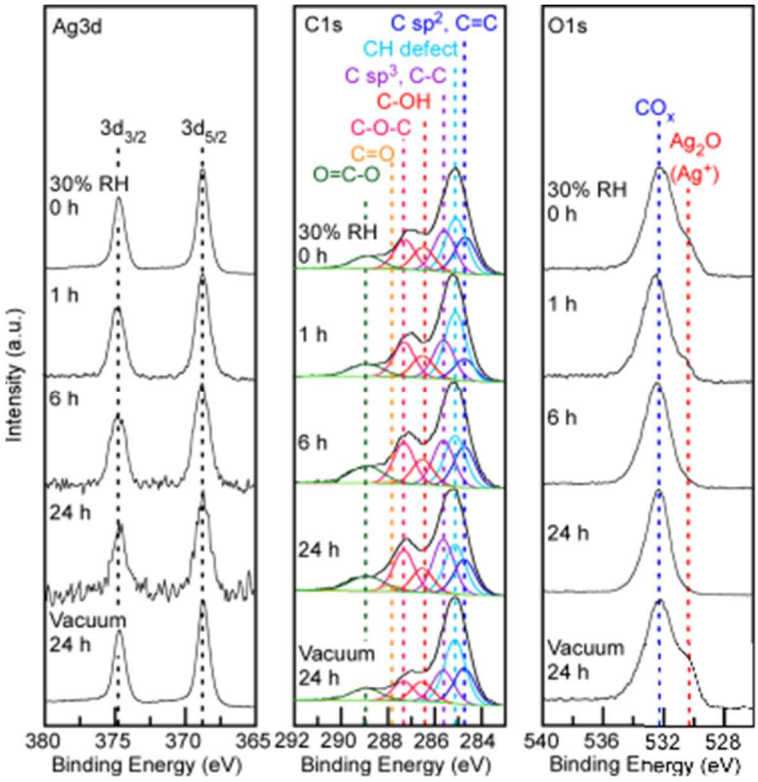

Figure 2-7. Time dependences of XPS spectra of Ag3d, C1s, and O1s at the Ag(17 nm)/GO interface under 30% RH and vacuum. Epoxide groups (C1s) remained even after 24 h under 30% RH. According to the O1s spectra, Ag_2O (Ag^+) was formed, and its peak intensity decreased with time because of Ag^+ permeation into the GO bulk under 30% RH. In contrast, this peak intensity was retained even after 24 h under vacuum because permeation into the GO bulk barely occurred under vacuum.

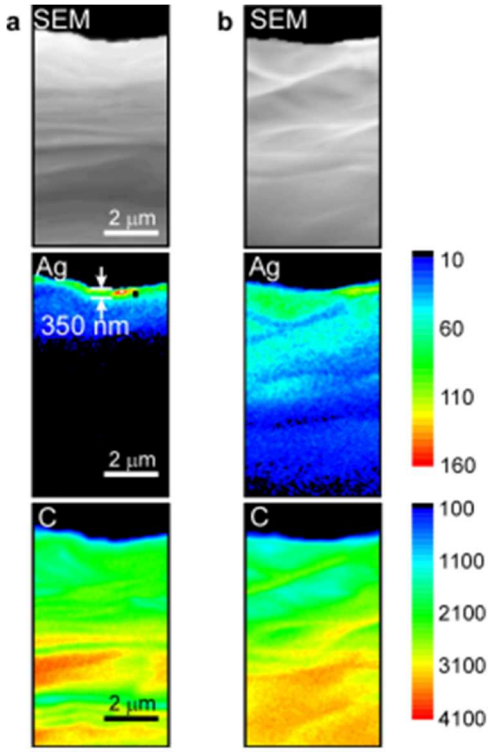

Figure 2-8. Cross-sectional SEM images and EPMA mappings of Ag and C. (a) As-deposited sample and (b) sample kept at 30% RH for 1 h. Scale bars denote the concentrations of Ag and C.

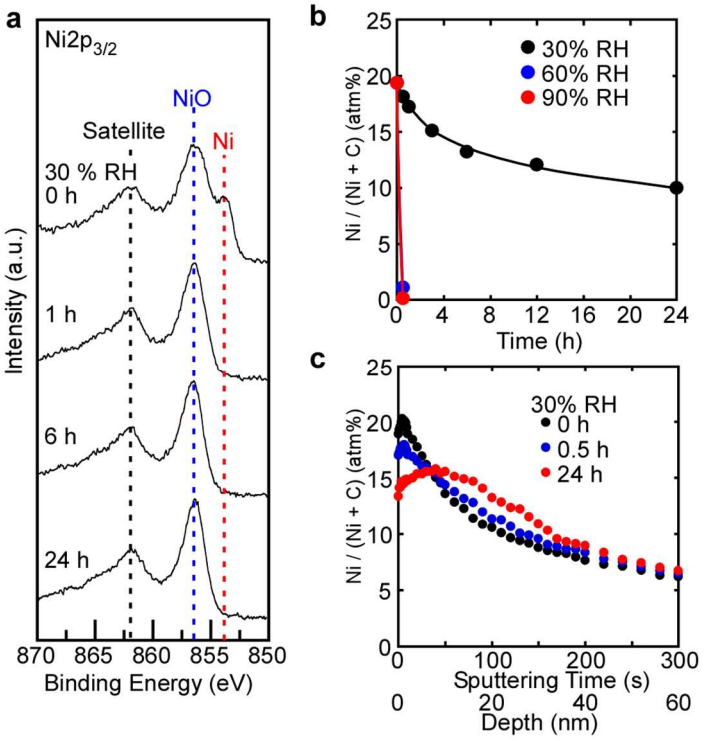

Figure 2-9. Time dependences of XPS spectra, surface content of Ni, and depth profiles of Ni in the Ni(17 nm)/GO sample. (a) Time dependences of XPS spectra of $Ni2p_{3/2}$ at the Ni/GO interface under 30% RH. Ni metal changed to Ni^{2+} (NiO) under 30% RH immediately after sputtering. (b) Ni content at the Ni/GO interface as a function of time under humid conditions. Ni content drastically decreased with time under 60% and 90% RH, compared with that under 30% RH. (c) Depth profiles of the Ni content at the Ni/GO interface at various times under 30% RH. After 30 min, Ni permeated the GO bulk.

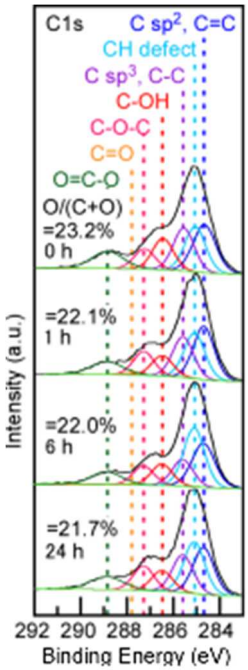

Figure 2-10. Time dependences of XPS spectra of C1s at the Ni(17 nm)/GO interface under 30% RH. Oxygen content decreased with time.

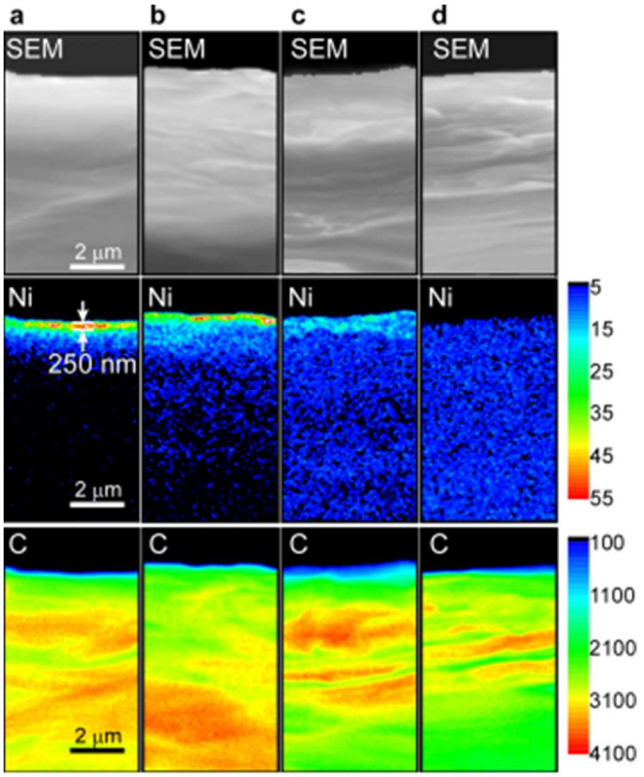

Figure 2-11. Cross-sectional SEM images and EPMA mappings of Ni and C. (a) As-deposited sample, sample kept at (b) 30% RH for 1 h, (c) 90% RH for 10 min, and (d) 90% RH for 1 h. Scale bars denote the concentrations of Ni and C.

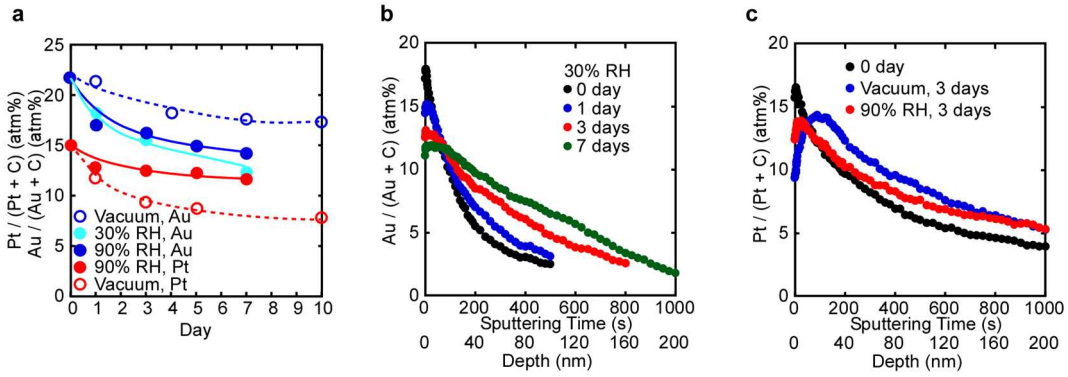

Figure 2-12. Surface content and depth profiles of Au and Pt in the Au(17 nm)/GO and Pt(17 nm)/GO samples, respectively. (a) Au and Pt content at the Au/GO and Pt/GO interfaces, respectively, as a function of time under humid conditions and vacuum. The Au content decreased with time under humid conditions, but barely did so under vacuum; in contrast, the Pt content decreased under vacuum but barely did so under 90% RH. (b) Depth profiles of the Au content at the Au/GO interface at various times under 30% RH. Au permeated the GO paper from the surface to around 200 nm into the GO bulk after 7 days. (c) Depth profiles of the Pt content at the Pt/GO interface at various times under 90% RH and vacuum. Pt permeated into the GO bulk after several days under vacuum.

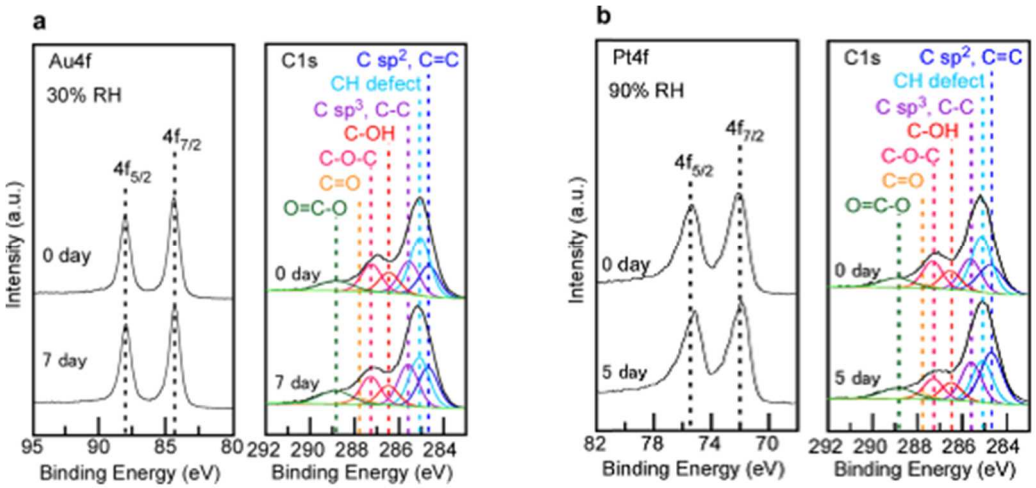

Figure 2-13. Time dependences of XPS spectra of Au4f, Pt4f, and C1s at the Au/GO (under 30% RH) and Pt/GO (under 90% RH) interfaces. (a) XPS spectra of Au4f and C1s at the Au/GO interface. (b) XPS spectra of Pt4f and C1s at the Pt/GO interface. Both Au and Pt were present in metal form, and the composition of the oxygenated groups barely changed with time.

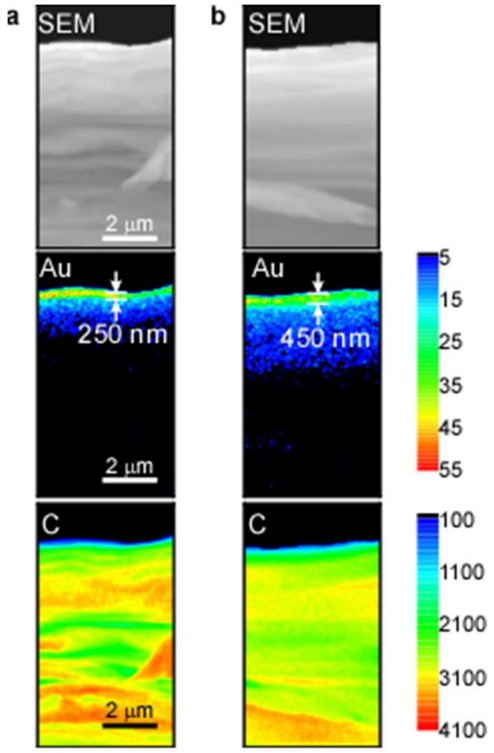

Figure 2-14. Cross-sectional SEM images and EPMA mappings of Au and C. (a) As-deposited sample and (b) sample kept in vacuum for 10 days. Scale bars denote the concentration of Au and C.

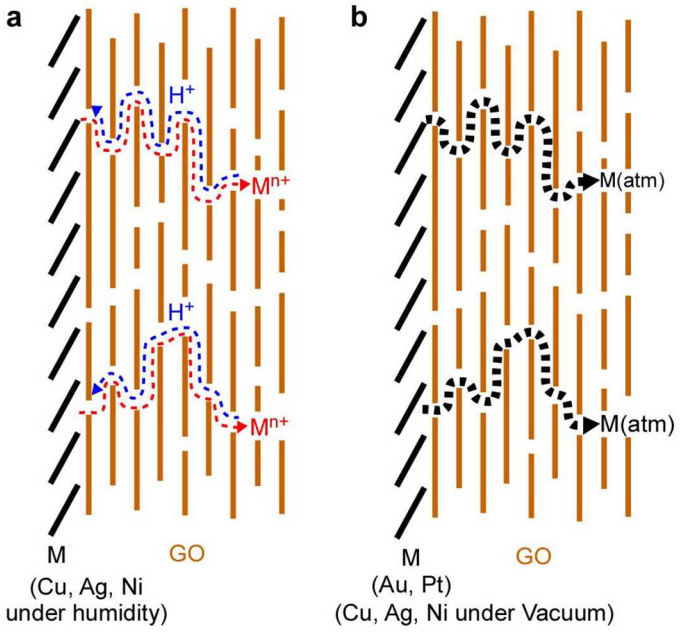

Figure 2-15. Permeation models for Cu, Ag, Ni, Au, and Pt metals. (a) Permeation model for Cu, Ag, and Ni. Metals are oxidized to the corresponding ions at the surface and then permeate into the GO bulk with simultaneous proton exchange. (b) Permeation model for Au and Pt, which permeate the GO bulk as atoms *via* defects and/or edges. Other metal (Cu, Ni, Ag) will diffuse as atoms with low diffusion rate.

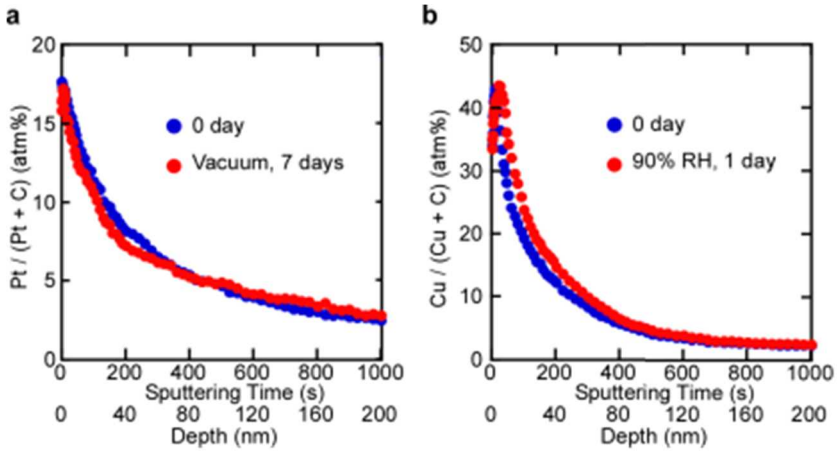

Figure 2-16. (a) Depth profiles of the Pt content at the Pt/HOPG interface after 7 days under vacuum. (b) Depth profiles of the Cu content at the Cu/HOPG interface after 1 h under 90% RH.

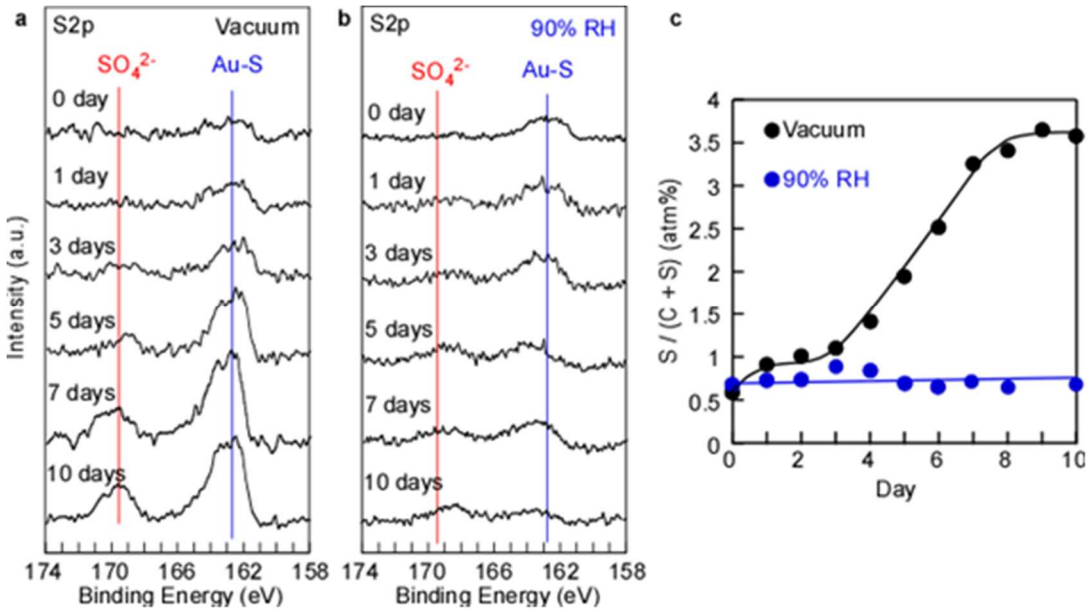

Figure 2-17. Time dependences of XPS spectra and surface content of S. Time dependences of S2p XPS spectra at the Au/GO interface under (a) vacuum and (b) 90% RH. (c) S content at the Au/GO interface as a function of time under vacuum and 90% RH.

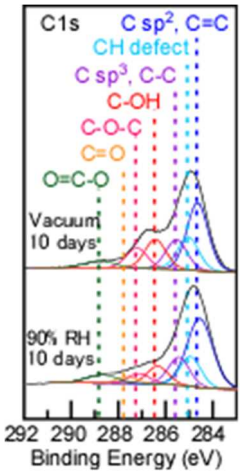

Figure 2-18. C1s XPS spectra at the Pt(17 nm)/GO interface under 90% RH and under vacuum for 10 days.

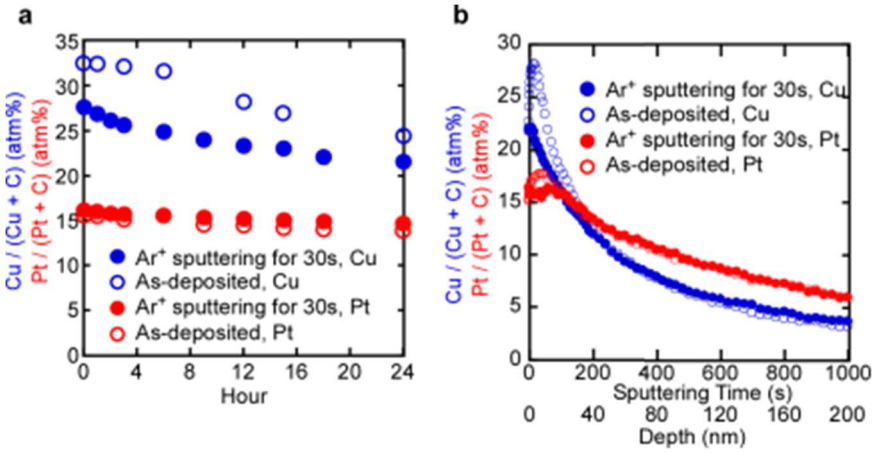

Figure 2-19. (a) Cu and Pt content at the Cu/GO and Pt/GO interfaces, respectively, as a function of time under vacuum. (b) Depth profiles of the Cu and Pt content at the Cu/GO and Pt/GO interfaces, respectively, after 1 day under vacuum.

References

(1) X. Chen, G. Wu, J. Chen, X. Chen, Z. Xie, and X. Wang, *J. Am. Chem. Soc*., 2011, **133**, 3693-3695.

(2) C. Zhu, L. Han, P. Hu and S. Dong, *Nanoscale*, 2012, **4**, 1641-1646.

(3) A. Dimiev, D. V. Kosynkin, A. Sinitskii, A. Slesarev, Z. Sun, and J. M. Tour, *Science*, 2011, **331**, 1168-1172.

(4) D. Chen, H. Feng, and J. Li, *Chem. Rev*., 2012, **112**, 6027-6053.

(5) M. Koinuma, C. Ogata, Y. Kamei, K. Hatakeyama, H. Tateishi, Y. Watanabe, T. Taniguchi, K. Gezuhara, S. Hayami, A. Funatsu, M. Sakata, Y. Kuwahara, S. Kurihara, and Y. Matsumoto, *J. Phys. Chem. C*, 2012, **116**, 19822-19827.

(6) Y. Matsumoto, H. Tateishi, M. Koinuma, Y. Kamei, C. Ogata, K. Gezuhara, K. Hatakeyama, S. Hayami, T. Taniguchi, A. and Funatsu, *J. Electroanal. Chem*., 2013, **704**, 233-241.

(7) K. T. Chan, J. B. Neaton, and M. L. Cohen, *Phys. Rev. B*, 2008, **77**, 235430-235441.

(8) A. V. Krasheninnikov, P. O. Lehtinen, A. S. Foster, P. Pyykko, and R. M. Nieminen, *Phys. Rev. Lett*., 2009, **102**, 126807-126810.

(9) D. W. Boukhvalov, and M. I. Katsnelson, *Appl. Phys. Lett*., 2009, **95**, 023109-02311.

(10) E. J. Kan, H. J. Xiang, J. Yang, and J. G. Hou, *J. Chem. Phys*., 2007, **127**, 164706-164710.

(11) H. Sevincli, M. Topsakal, E. Durgun, and S. Ciraci, *Phys. Rev. B*, 2008, **77**, 195434-195440.

(12) V. A. Rigo, T. B. Martins, A. J. R. da Silva, A. Fazzio, and R. H. Miwa, *Phys. Rev. B*, 2009, **79**, 075435-07543.

(13) P. Jensen, X. Blase, and P. Ordejon, *Surf. Sci*., 2004, **564**, 173-178.

(14) J. Akola and H. Hakkinen, *Phys. Rev. B*, 2006, **74**, 165404-165412.

(15) S. Malola, H. Hakkinen, and P. Koskinen, *Appl. Phys. Lett.*, 2009, **94**, 043106-043108.

(16) W. H. Brito and R. H. Miwa, *Phys. Rev. B*, 2010, **82**, 045417-045423.

(17) Y. Gan, L. Sun, and F. Banhart, *Small*, 2008, **4**, 587-591.

(18) R. Anton and P. Kreutzer, *Phys. Rev. B*, 2000, **61**, 16077-16083.

(19) W. S. Hummers Jr., R. E. Offeman, *J. Am. Chem. Soc*., 1958, **80**, 1339.

(20) A. Zalar, J. Kovac, B. Pracek, P. Panjan, and M. Ceh, *Appl. Surf. Sci*., 2008, **254**, 6611-6618.

(21) M. P. Seah, *Thin Solid Films*, 1981, **81**, 279-287.

(22) G. K Wehner, *Methods of Surface Analysis*. In: The aspects of sputtering in surface analysis methods. (Czanderna, A. W., ed.) 1-37 (Elsevier Scientific Publishing Company, Amsterdam, Oxford, and New York, 1975).

(23) M. Koinuma, H. Tateishi, K. Hatakeyama, S. Miyamoto, C. Ogata, A. Funatsu, T. Taniguchi, and Y. Matsumoto, *Chem. Lett*., 2013, **42**, 924-926.

(24) A. Buchsteiner, A. Lerf, and J. Pieper, *J. Phys. Chem. B*, 2006, **110**, 22328-22338.

(25) M. R. Karim, K. Hatakeyama, T. Matsui, H. Takehira, T. Taniguchi, M. Koinuma, Y. Matsumoto, T. Akutagawa, T. Nakamura, S. Noro, T. Yamada, H. Kitagawa, and S. Hayami, *J. Am. Chem. Soc*., 2013, **153**, 8097-8100.

(26) A. Maiti, and A. Ricca, *Chem. Phys. Lett*., 2004, **395**, 7-11.

(27) I. Suarez-Martinez, A. Felten, J. J. Pireaux, C. Bittencourt, and C. P. Ewels, *J. Nanosci. Nanotechnol*., 2009, **9**, 6171-6175.

(28) Y. Tang, Z. Yang, and X. Dai, *J. Chem. Phy*s., 2011, **135**, 224704-224710.

(29) R. Anton and I. Schneidereit, *Phys. Rev. B*, 1998, **58**, 13874-13881.

(30) C. A. Lang, M. M. Dovek, J. Nogami, C. F. Quate, C. A. Lang, M. M. Dovek, J. Nogami, and C. F. Quate, *Surf. Sci*., 1989, **224**, L947-L955.

(31) P. A. Pandey, G. R. Bell, J. P. Rourke, A. M. Sanchez, M. D. Elkin, B. J. Hickey, and N. R. Wilson, *Small*, 2011, **7**, 3202-3210.

(32) J. K. Bal and S. Hazra, *Phys. Rev. B*, 2007, **75**, 205411-205416.

(33) K. Raidongia and J. Huang, *J. Am. Chem. Soc*., 2012, **134**, 16528-16531.

(34) P. Sun, M. Zhu, K. Wang, M. Zhong, J. Wei, D. Wu, Z. Xu, and H. Zhu, *ACS Nano*, 2013, **7**, 428-437.

(35) P. G. Lustemberg, C. Vericat, G. A. Benitez, M. E. Vela, N. Tognalli, A. Fainstein, M. L. Martiarena, and R. C. Salvarezza, *J. Phys. Chem. C*, 2008, **112**, 11394-11402.

(36) R. V. Hull, L. Li, Y. Xing, and C. C. Chusuei, *Chem. Mater*., 2006, **18**, 1780-1788.

(37) C. Xu, X. Wang, and J. Zhu, *J. Phys. Chem. C*, 2008, **112**, 19841-19845.

(38) R. R. Nair, H. A. Wu, P. N. Jayaram, I. V. Grigorieva, and A. K. Geim, *Science*, 2012, **335**, 442-444.

CHAPTER 3

All-graphene oxide device with tunable supercapacitor and battery behaviour by the working voltage

Overview

We propose a new type of all-graphene oxide device. Reduced graphene oxide (rGO)/graphene oxide (GO)/rGO functions as both a supercapacitor and a battery, depending on the working voltage. The rGO/GO/rGO operates as a supercapacitor until 1.2 V. At greater than 1.5 V, it behaves as a battery using redox reaction.

3.1. Introduction

The global energy paradigm is rapidly transforming from fossil fuels to sustainable energy resources, including solar, wind and geothermal sources.[1] However, power production from these energy resources is not always coincident with energy demand. Therefore, the development of large-scale energy storage systems that resolve this discrepancy is important. Considerable efforts have been expended on the development of high-performance energy storage devices such as Li-ion batteries (LIBs) and supercapacitors (SCs).[2,3] LIBs can commonly deliver a high energy density (150–200 Wh kg^{-1}), but are limited by their low power density (less than 1000 W kg^{-1}) and poor cycling lifetime (less than 1000 cycles).[2,4] In contrast, SCs can deliver much higher power density (5–10 kW kg^{-1}) and exhibit long cycle stability (exceeding 1×10^5 cycles) but suffer from a much lower energy density (less than 10 Wh g^{-1}).[5] Accordingly, a new energy storage device with the combined characteristics of high energy and power densities and long cycle life is strongly desired as a solution to bridge the gap between LIBs and SCs.[6] In addition, such energy storage devices should preferably be composed of inexpensive, easily acquired materials and be capable of being

fabricated through a relatively simple manufacturing process.

Graphene oxide (GO) has recently attracted extensive attention because it offers a low-cost, scalable and wet-chemical approach to graphene. Furthermore, GO exhibits excellent membrane properties, including high water permeability,[7] good ion and gas selectivity[8] and high proton conductivity;[9] these properties arise from the presence of various oxygenated functional groups. These advantages have led to the application of GO as a solid electrolyte for SCs[10,11] and batteries (*e.g.* fuel cells,[12] lead–acid batteries[13] and Li–S batteries[14]). In comparison, reduced GO (rGO), which exhibits high electric conductivity and high specific surface area (SSA), can be used in various electrodes of electrical devices such as LIBs, SCs and hybrid Li-ion capacitors.[2,3,15] Although most GO based devices are fabricated either with GO as the electrolyte or with an rGO electrode, an rGO/GO/rGO hybrid structure, which comprises GO electrolyte/separator and rGO electrodes, is attractive because of the potential to develop an all-carbon energy device. Such a research direction has been introduced in the literature; however, only the capacitive behaviours of the rGO/GO/rGO structure have been investigated.[10] Its redox behaviours have not yet been focused on, despite the promising applications in energy storage devices.

In this study, we demonstrate a new type of rGO/GO/rGO device that exhibits both supercapacitor and battery behaviour. This device was easily fabricated *via* photoirradiation of both surfaces of a GO film in a single step. This work, as a solution to bridge the gap between batteries and SCs, sheds new light on the development of energy storage devices.

3.2. Experimental Section

3.2.1. Synthesis of graphene oxide

The graphene oxide (GO) was prepared from natural graphite powder (special grade reagent, Wako Ltd.) by Hummers' method.[16] Graphite powder (2.0 g), $NaNO_3$ (2 g, special reagent, Wako Ltd.) and

98% H_2SO_4 (92 mL, special reagent, Wako Ltd.) were mixed at 0 °C in an ice-water bath. $KMnO_4$ (12 g, special reagent, Wako Ltd.) was added slowly. The reaction mixture was removed from the ice-water bath and stirred to oxidise the graphite powder for 45 min at 95 °C. The resulting mixture was diluted with distilled water, and 30% H_2O_2 (5 mL, special reagent, Wako Ltd.) was added to neutralise any remaining $KMnO_4$. The product was washed with 5% HCl (special reagent, Wako Ltd.), centrifuged several times at 3,000 rpm to remove excess HCl and dried in an oven at 70 °C for 7 days. GO was suspended in distilled water by bath sonication for 2 h, and the resulting suspension was ultracentrifuged at 10,000 rpm. The supernatant was used as the GO suspension.

3.2.2. Preparation of GO paper

The GO suspensions (4 mg mL^{-1}, 20 mL) were filtered using a membrane filter (0.4 μm pore size, Merck Millipore) under reduced pressure overnight and then peeled from the filter, resulting in free-standing and flexible GO paper.

3.2.3. Fabrication of reduced GO/GO/ reduced GO devices

The reduced GO (rGO)/GO/rGO structure was fabricated by photoirradiation of both surfaces of the GO paper for 1 to 12 h in air using a 500 W (32.5 mW cm^{-2}) high-pressure mercury lamp (USHIO, SX-U1501HQ). Au was sputter-coated onto both surfaces of the rGO/GO/rGO film using a sputtering machine (K575K, Emitech) to improve the contact. Photoreduction and Au sputtering were performed using a mask to define the electrode area (diameter circle: 1 cm).

3.2.4. Characterisation

The morphology of the samples was verified using field-emission scanning electron microscope (FE-SEM; Hitachi High-Tech, SU-8000). X-ray photoelectron spectroscopy (XPS, Thermo

Scientific, Sigma Probe) was used to determine the degree of oxidation of the samples. Thermogravimetric analysis (TGA) curves were generated using a thermal analyser (Seiko Instruments, EXSTAR 6000). The experiments were designed from room temperature to 1,000 °C at a heating rate 4 °C min^{-1} under nitrogen protection. To exclude the moisture desorption below 100 °C, the obtained results were analysed above that temperature.[17]

3.2.5. Electrochemical characterisation of rGO/GO/rGO devices

The electrochemical performance of the rGO/GO/rGO devices was investigated using cyclic voltammetry (CV), galvanostatic charge/discharge (CC) measurements and electrochemical impedance spectroscopy (EIS). CV and CC measurements were performed on an electrochemical workstation (IVIUM TECHNOLOGIES, CompactStat). EIS measurements were recorded on an impedance/gain phase analyser (Solartron 1260) over the frequency range from 2 MHz to 0.01 Hz with an amplitude of 50 mV. All experiments were performed at 25 °C 40% after being maintained for 1 h under ambient conditions to become stable.

3.2.6. Calculations

3.2.6.1. Capacitance

The capacitance was calculated from the CV and CC data according to the following formula:

$$C_{device} = \frac{I}{dV/dt} \quad ,$$

where *I* refers to the mean current in the CV curves and the set current in CC, and *dV/dt* refers to the scan rate in the CV curves or to the slope of the discharge curves in CC.

Specific capacitances were calculated on the basis of the area or the volume of the device stack according to the following formulas:

$$\text{Areal capacitance} = \frac{C_{device}}{A} \quad ,$$

$$\text{Volumetric stack capacitance} = \frac{C_{device}}{V} \quad ,$$

where A refers to the total surface area (cm^2) of the positive and negative electrode and V refers to the volume (cm^3) of the device. The stack capacitances (F cm^{-3}) were calculated with the volume of the device taken into account, including the rGO, GO and Au current collector. The rGO electrodes were typically circular, with a diameter of 1 cm. In the rGO/GO/rGO devices, A was $2 \times 0.5^2 \times \pi$ (cm^2) and V was $0.5^2 \times \pi \times$ thickness of the rGO/GO/rGO device (cm^3).

The power density of the devices was calculated from the galvanostatic curves at different CC current densities using the following formula:

$$P_{max} = \frac{\Delta E^2}{4 R_{ESR} V} \quad ,$$

where P is the power density (W cm^{-3}), ΔE is the operating voltage window (measured in volts and obtained from the discharge curve excluding the IR drop) and V is the volume of the device as indicated earlier (in cm^3). Parameter R_{ESR} is the internal resistance of the device, which was estimated from the voltage drop at the beginning of the discharge, V_{drop}, at a constant current density (i) using the equation

$$R_{ESR} = \frac{V_{drop}}{2i} \quad .$$

The energy density of the device was obtained from the formula

$$E = \frac{C_V \times \Delta E^2}{2 \times 3600} \quad ,$$

where E is the energy density (Wh cm^{-3}), C_V is the volumetric stack capacitance and ΔE is the operating voltage window in volts (measured in volts and obtained from the discharge curve, excluding the IR drop).

3.2.6.2. Mass of rGO electrode

Assuming that there is no involvement of other types of elements (such as hydrogen, 2H + O → H_2O) and that two oxygen atoms will react with one carbon atom to de-functionalise at a high temperature,

$$C + 2O \rightarrow CO_2$$

According to XPS results, the atomic ratio of oxygen is 39%, the atomic ratio of carbon is 61%, and all oxygen leaves the sample in the form of carbon dioxide. Thus,

$$Wt\%_{left} = 1 - Wt\%_{burned} = 1 - \frac{weight_{burn}}{weight_{starting}}$$

$$= 1 - \frac{weight_{carbonburned} + weight_{oxygenburned}}{weight_{carbonstarting} + weight_{oxygenstarting}}$$

$$= 1 - \frac{\left(\frac{0.39}{2}\right) \times 12 \ \ g \cdot mol^{-1} + 0.39 \times 16 \ \ g \cdot mol^{-1}}{0.61 \times 12 \ \ g \cdot mol^{-1} + 0.39 \times 16 \ \ g \cdot mol^{-1}}$$

$$= 36.73 \ \ wt\%$$

TGA measurement reveals that 35.77 wt% is left of the GO film, which is close to the calculated value of 36.73 wt%.

Similarly, according to XPS results, the atomic oxygen ratio is 23% for the rGO external layer. Thus,

$$Wt\%_{left} = 1 - Wt\%_{burned} = 1 - \frac{weight_{burn}}{weight_{starting}}$$

$$= 1 - \frac{weight_{carbonburned} + weight_{oxygenburned}}{weight_{carbonstarting} + weight_{oxygenstarting}}$$

$$= 1 - \frac{\left(\frac{0.23}{2}\right) \times 12 \ \ g \cdot mol^{-1} + 0.23 \times 16 \ \ g \cdot mol^{-1}}{0.77 \times 12 \ \ g \cdot mol^{-1} + 0.23 \times 16 \ \ g \cdot mol^{-1}}$$

$$= 60.84 \ \ wt\%$$

Therefore, after de-functionalisation at high temperature in TGA, assuming that the sandwiched GO film is with α wt% of rGO external layers and (100 − α) wt% of GO intralayers, the percentage P of left weight can be calculated as

$$P = \alpha\ \ wt\% \times 60.84\ \ wt\%\ \ + (1 - \alpha\ \ wt\%) \times 36.73, and\ \ P = 36.75\ \ wt\%$$

Thus, rGO external layers occupy a weight percentage α wt% = 0.8 wt% in GOSC-6 h.

3.2.7. Electron conductivity measurement of GO and rGO films

The electron conductivities of the samples were measured by a four-probe DC method using an electrochemical workstation (IVIUM TECHNOLOGIES, CompactStat). The four-probe measurement with a BT-115 conductivity cell (ElectroChem, Inc.) was performed on a single piece of GO film with a thickness of 50 μm. The spacing between each probe was 0.5 cm, and the length of each probe was 2.0 cm.

The corresponding electron conductivity was calculated from the resistance value according to the following formula:

$$\sigma = \frac{d}{R\ \times\ T\ \times\ L}\ \ ,$$

where σ is the electron conductivity, d is the width (the distance between the electrodes, 0.5 cm), R is the resistance value in Ω obtained from the I–V curve, T is the thickness of the GO film in cm and L is the length of the membrane (1 cm). The calculated electron conductivity is expressed in units of S cm^{-1}.

3.3. Results and Discussion

Figure 3-1 illustrates the fabrication steps of the rGO/GO/rGO device. When both surfaces of a GO film were photoirradiated under ambient conditions, the GO film converted into rGO/GO/rGO in a single step (Figure 3-2). Two-sided rGO, which exhibits electrical conductivity, serves as the electrodes. A GO interlayer is retained in the middle and functions as a solid-state electrolyte/separator because of its good ionic conductivity and electronic insulating properties. Moreover, this all-solid-state device is thin (approximately 50 μm) and completely flexible (Figure

3-3).

To investigate the effect of the photoreduction step, we prepared rGO/GO/rGO using various photoreduction times ranging from 0 to 12 h and tested the electrochemical performance of the resulting devices in the potential window between 0 and 1 V at various scan rates. The cyclic voltammetry (CV) profiles are all rectangular in shape (see Figure 3-4a and Figure 3-5a–e), which indicates good double-layer capacitive behaviour. We refer to this device consisting of rGO/GO/rGO as a graphene oxide supercapacitor (GOSC). Compared with other GO-based micro-supercapacitors,[10,17] GOSC exhibited excellent rate performance (Figure 3-5f). This trend confirms that the rGO electrode of GOSC is highly accessible to electrolyte ions such as protons, thus providing high capacitance even when operated at 1000 mV s^{-1}. The specific capacitance increases with increasing photoreduction time (Table 3-1). GOSC constructed with photoreduction time of 6 h (GOSC-6 h) exhibits the highest specific areal capacitance of 2 mF cm^{-2}. The lower capacitance for GOSC-12 h compared to that for GOSC-6 h is attributed to an increase in the electronic conductivity of the GO interlayer.

Because GOSC-6 h exhibited the highest specific capacitance among the fabricated GOSCs, all subsequent electrochemical measurements were carried out on GOSC-6 h. Galvanostatic charge/discharge (CC) curves at different current densities are shown in Figure 3-4b and Figure 3-6. All the curves are nearly isosceles triangles, which indicates high coulombic efficiency and standard double-layer capacitor behaviour. The cyclic stability tests performed on GOSC-6 h are shown in Figure 3-4c. After 60 CC cycles at a current density of 0.1 mA, the device retained approximately 80% of its original capacitance. To investigate the cause of capacitance degradation, GOSC-6 h after 100 charge/discharge cycles was analysed by X-ray photoelectron spectroscopy (XPS) (Figure 3-7). The CH defect of the rGO electrodes converted into C=C and the oxygenated functional groups (particularly, the COC epoxide) of the GO interlayer slightly decreased after 100 charge/discharge

cycles. We speculate that the main reasons of capacitance degradation were (1) the decreasing CH defects, which were functioned as active sites of the rGO electrode, and (2) the decreasing electrical insulating property and proton conductivity because of the decreasing oxygenated functional groups of the GO interlayer.

Electrochemical impedance spectroscopy further confirms the superior performance of GOSC (Figure 3-4). The equivalent series resistance obtained from the intercept of the plot on the real axis at high frequency is approximately 80 Ω, which represents the intrinsic internal resistance of the rGO electrode and the GO electrolyte/separator of GOSC; this resistance reflects the good ionic conductivity of the electrolyte and the low internal resistance of the electrodes. The semicircles at the middle frequency range, which are related to the nature of the interface between GO electrolyte/separator and the rGO electrode (*i.e.* charge-transfer resistance), decrease with increasing photoreduction time because of the increasing electronic conductivity of rGO. The XPS results and current–voltage (*I–V*) curves confirm this behaviour (Figure 3-2 and 3-8). Moreover, GOSC exhibits superior frequency response, with an extremely short relaxation time (Figure 3-9). The RC time constant of GOSC-6 h was calculated to be 2.2 s, in comparison with 10 s for a commercial activated-carbon supercapacitor.[18] In addition, GOSC-6 h exhibits a small leakage current of 128 nA after 12 h (Figure 3-10). A summary of electrochemical performance of GOSC is provided in Table 3-1. Figure 3-12 shows a Ragone plot comparing the performance of GOSC obtained by various photoreduction times. It reveals a significant increase in the supercapacitor performance with increasing photoreduction times. Notably, the energy density for GOSC-6 h is calculated to be 1.1×10^{-4} Wh cm^{-3}, with a power density of 0.12 W cm^{-3}.

Gao *et al.* fabricated GO-based micro-supercapacitor using a laser technique to write rGO patterns directly on GO films.[10] They reported high specific capacitances of 0.26–0.86 mF cm^{-2} for their micro-supercapacitors. Notably, although laser treatment results in an increase in the SSA and

electrical conductivity of rGO, the capacitance of the GO-based micro-supercapacitor is approximately equal to or less than the 2 mF cm^{-2} capacitance exhibited by GOSC-6 h.

Given the aforementioned results, surface chemistry rather than SSA is the determining factor for the high capacitive performance of GOSC. In the case of GOSC, the rGO with minimal oxygenated functional groups provides a charged surface area, which strongly affects the wettability of the rGO surfaces accessible to electrolyte ions such as protons. Moreover, we and others have reported that graphite materials with defects such as CH and pentagon–heptagon pairs can deliver higher capacitance than perfect defect-free graphitic materials.[19] In our case, the XPS spectra showed that the content of COC and C=O groups decreased, whereas that of the C=C groups and CH defects increased after the photoreduction (Figure 3-2). Thus, the rGO structure, which contains minimal oxygenated functional groups and an abundance of defects, is responsible for the devices' high capacitance.

Later, Zhang *et al.* interpreted the capacitive behaviour of GO-based micro-supercapacitor.[17] From molecular dynamic simulations and the anomalous environment of GO interlayers, they proposed a new capacitive model that combines the two distinct charge storage mechanisms of dielectric capacitors and electrochemical capacitors. Therefore, we speculate that the charge storage mechanism of GOSC results from (1) proton conductivity and (2) polarised/separated water molecules in the interlayer spacing of the nanoscale GO.

The fabrication of an all-graphene oxide redox battery (GORB) is a challenge in the field of electronic and energy storage devices. The operation of GO-based devices in a voltage window of *ca.* 2 V has not yet been well developed because the cell voltage of aqueous-electrolyte-based GO devices is usually restricted to 1 V; this narrow voltage window is based on the decomposition voltage of water at 1.23 V.

The rGO/GO/rGO constructed with a photoreduction time of 1 h was measured at

potentials higher than 1 V (Figure 3-13a and Figure 3-14). The CC curves were nearly isosceles triangles until 1.2 V; this shape corresponds to capacitive behaviour, which defines GOSC, as previously discussed. At potentials higher than 1.5 V, a voltage plateau was observed during charge/discharge. Although the plateau potential exhibited an increase in voltage from 1.5 to 2.0 V, the charge voltage of 2.0 V resulted in a large decrease of coulombic efficiency (72% at 1.7 V; 9% at 2.0 V) and discharge time after five cycles (Figure 3-14). This phenomenon indicates that the hydrogen production reaction proceeded during charging at potentials greater than 1.7 V. In addition, the carboxyl group, which is one of the least conductive functional groups and exhibits little reversible redox ability, and CO_2 evolution may result in degradation at 2.0 V.[20] Thus, charge voltages greater than 1.7 V are not suitable for stable operation of GORB.

To understand the effect of photoreduction, we fabricated GORB using various photoreduction times ranging from 0 to 6 h and tested their electrochemical performance in the potential window of 0 to 1.7 V at 0.05 mA (Figure 3-13b and Figure 3-15). The plateau potential and charge/discharge time increased with increasing photoreduction time. Excellent performance was observed for GORB prepared with a photoreduction time of 3 h (GORB-3 h). Under the hypothesis that the decrease of the charge/discharge time for GORB-6 h is a consequence of its relatively small number of oxygenated functional groups involved in the redox reaction, we conducted further experiments on GORB-3 h.

Figure 3-13c and d show typical CV and CC results, respectively, for GORB-3 h. The plateau potential of GORB-3 h observed at approximately 0.75 V corresponds to the difference in the redox potentials for the anode and the cathode. A coulombic efficiency of approximately 53% was obtained for the charge/discharge cycles of GORB-3 h. Figure 3-16 shows the cycle stability of GORB-3 h. Approximately 90% of the initial capacitance value of GORB-3 h is maintained after 100 charge/discharge cycles.

Figure 3-17 shows the XPS spectra for both the anode and the cathode of GORB-3 h after various charge/discharge cycles. The rGO of the cathode was extensively functionalised, whereas far less functionalisation was observed on the rGO anode. This result indicates that the rGO/GO/rGO device, which comprises two different rGO electrodes with redox couples based on two different functional groups with different reaction potentials, functions as a battery. In addition, analysis of the anode of GORB-3 h indicates that CH defects were the main products after 200 charge/discharge cycles. On the other hand, the contents of oxygenated functional groups in the rGO cathode were barely changed.

Recently, Tomai *et al.* demonstrated metal-free aqueous redox capacitors using anthraquinone (AQ: −0.16 V vs. Ag/AgCl) and tetrachlorohydroquinone (TCHQ: 0.50 V vs. Ag/AgCl) supported on nanoporous activated carbon.[21] Moreover, Kobayashi *et al.* demonstrated rechargeable proton exchange membrane fuel-cell batteries fabricated with a modified carbon anode and an RuO_2/C cathode. They attributed the plateau potential, which appeared at 0.85 V, to the potential difference between the carbonyl/phenol redox reaction on the surface of modified carbon (C–OH ↔ C=O + H^+ + e^-) and the oxygen evolution reaction ($4H^+ + 4e^- + O_2 \leftrightarrow H_2O$).[20]

On the basis of these results, we deduced the following two hypotheses for the redox mechanism of GORB: (1) cathode: C=O + H^+ + e^- ↔ C–OH; anode: CH (defect) + CO_2 ↔ 2C=O (or C–O) + H^+ + e^- ; or (2) cathode: $4H^+ + 4e^- + O_2 \leftrightarrow H_2O$; anode: CH (defect) + CO_2 ↔ 2C=O (or C–O) + H^+ + e^-. Researchers have devoted substantial effort to determining the redox potential of GO.[22] However, to our knowledge, the detailed redox centre and potential of the oxygenated functional groups on GO have not been elucidated. As quinone/hydroquinone molecules have various redox potentials,[23] determining the redox potential of the oxygenated functional groups on GO is inherently difficult. In our case, the oxygenated functional groups on the rGO behave as reactants are not conclusively known. However, as previously mentioned, we assume that the redox

couple could be quinone/hydroquinone derived from oxygenated functional groups on the rGO and/or the oxygen evolution reaction. Further investigations are ongoing to obtain more qualitative evidence with respect to how various factors influence the redox performance of GORB.

From a practical viewpoint, the performance of GOSC and GORB should be further improved. Nonetheless, our research demonstrates possibilities of using GOSC/GORB as an advanced energy storage device that can be operated at low temperature and low humidity. We expect that further control and modification of the oxygenated functional groups on GO will enable the fabrication of different types of batteries that operate *via* various redox reactions. In addition, the nanoscale interlayer of the GO film may serve as unique two-dimensional reaction fields, based on the high water permeability, water polarisation and ionic conductivity, leading to electronic devices that operate on a new mechanism arise.

3.4. Conclusion

In conclusion, the rGO/GO/rGO structure functions as both a supercapacitor and a battery under low-humidity and low-temperature conditions, depending on the working voltage. The rGO/GO/rGO structure behaves as a proton-type supercapacitor until 1.2 V. At potentials greater than 1.5 V, this device behaves as a battery operating on the redox reaction between the oxygenated functional groups at the rGO. Finally, the advantages of our proposed device over current energy storage devices are summarised as follows. First, our rGO/GO/rGO device operates without the use of external electrolytes and binders. Second, the simple fabrication process does not require additional processing or complex operations to produce a device that functions as both a supercapacitor and a battery. Third, stacking the device enables an increase in energy density while maintaining the ultrathin construction of the device. These advantages are attractive to develop novel carbon-based energy devices with low fabrication cost and high device performance.

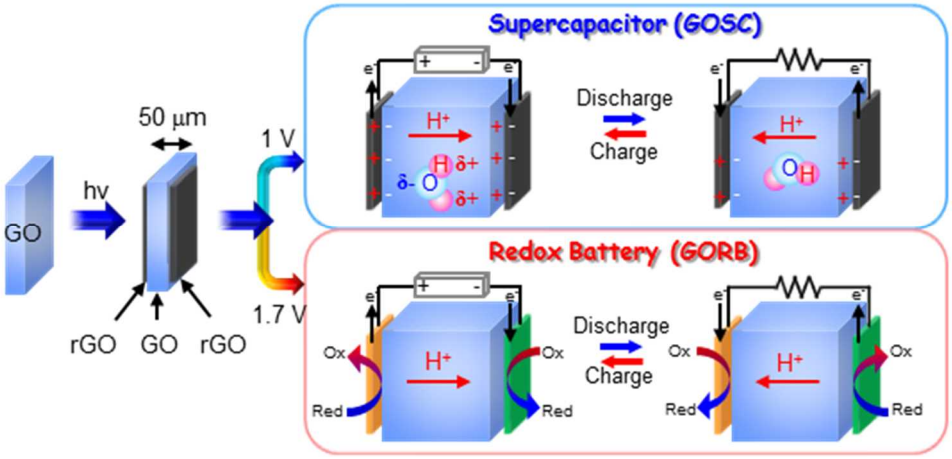

Figure 3-1. Schematic of the rGO/GO/rGO device.

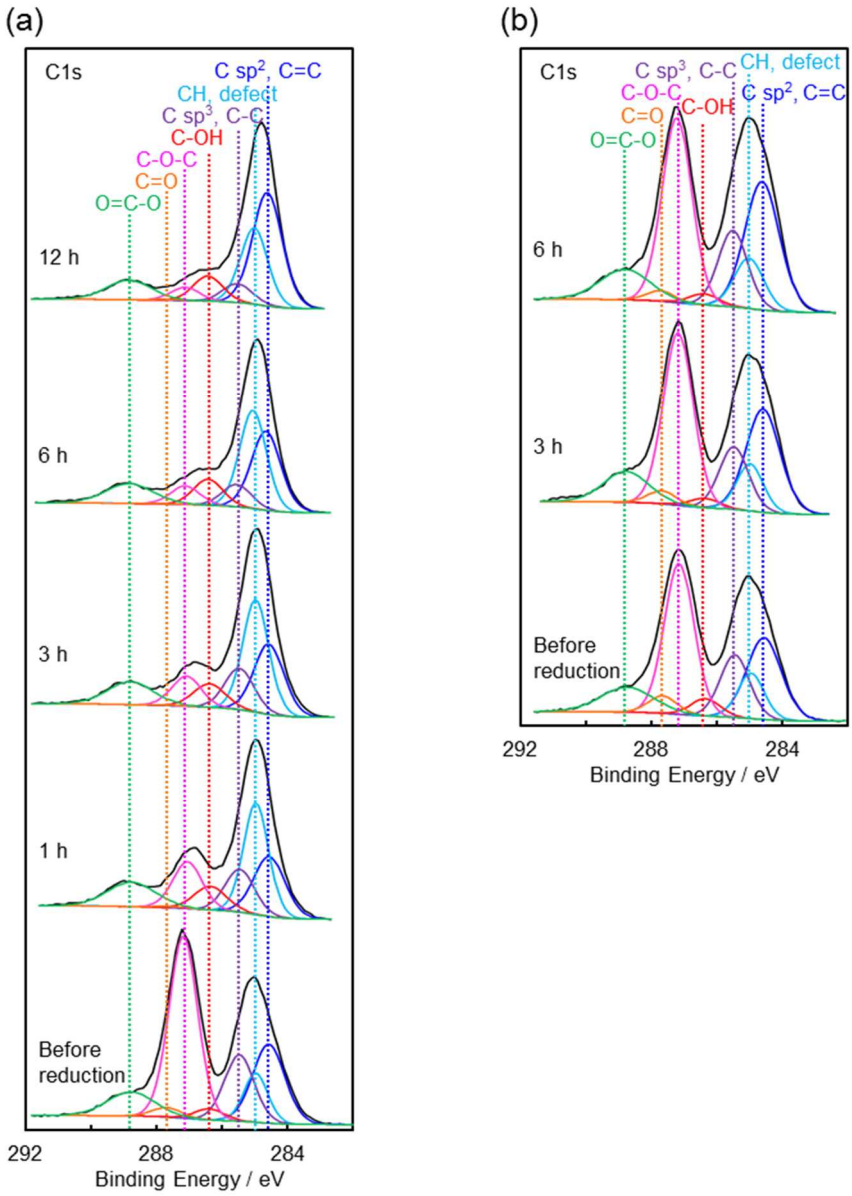

Figure 3-2. C 1s XPS spectra of (a) surface and (b) interlayer of rGO/GO/rGO at various photoreduction times. The interlayer of rGO/GO/rGO was obtained by peeling off the rGO layer using scotch tape. The C 1s XPS spectra were split into seven groups (–COOH, C=O, C–O–C, C–OH, sp^3 C–C, C–H defect and sp^2 C=C bonds).

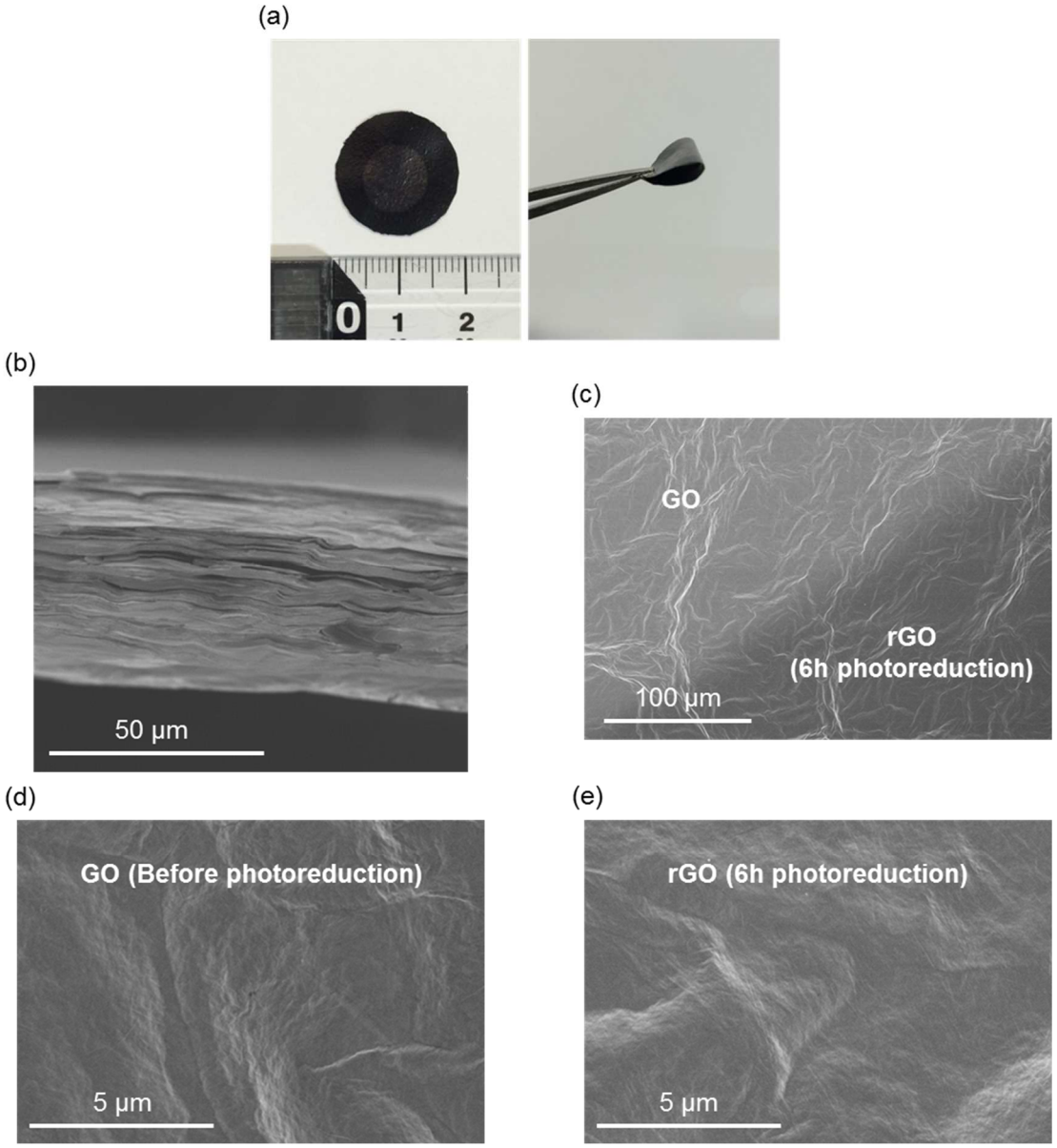

Figure 3-3. (a) A digital photograph of the rGO/GO/rGO device. (b) Cross-sectional SEM image of rGO/GO/rGO constructed with a photoreduction time of 6 h. Analysis of the cross section of this device reveals a thickness of approximately 50 μm. (c-d) Different magnification SEM images of GO/rGO boundary of the surface, GO surface and rGO surface. Because photoreduction was not associated with thermal effects,[10,17,18] the morphological change between GO and rGO was not observed clearly.

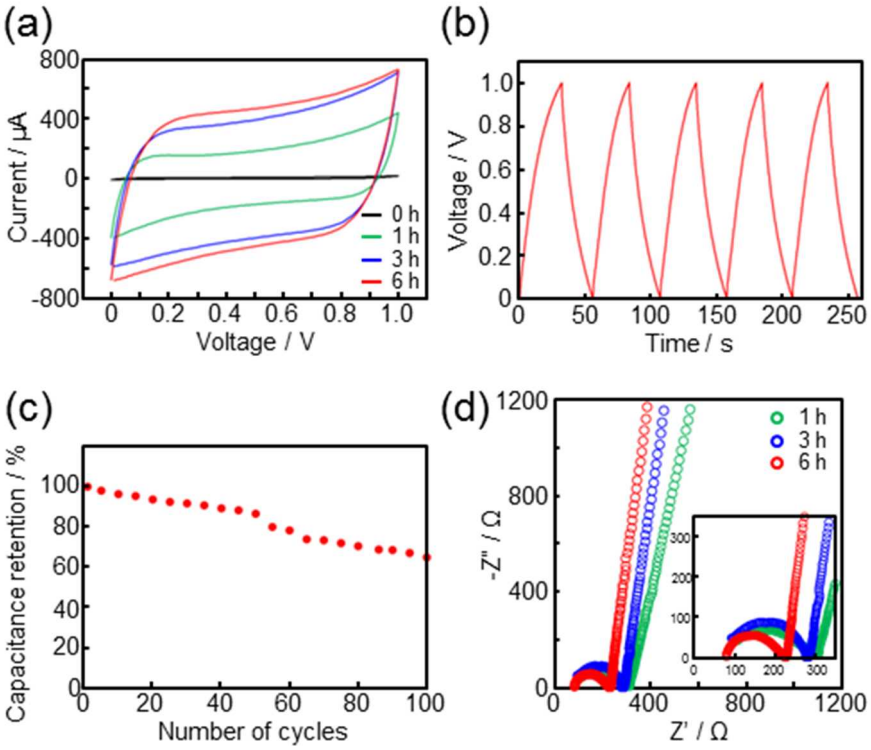

Figure 3-4. (a) CV profiles acquired at a scan rate of 0.3 V s^{-1} for the GOSC prepared using various photoreduction times. (b) CC of GOSC-6 h at 0.1 mA. (c) Performance durability of GOSC-6 h at 0.1 mA. (d) Impedance spectra at various photoreduction times.

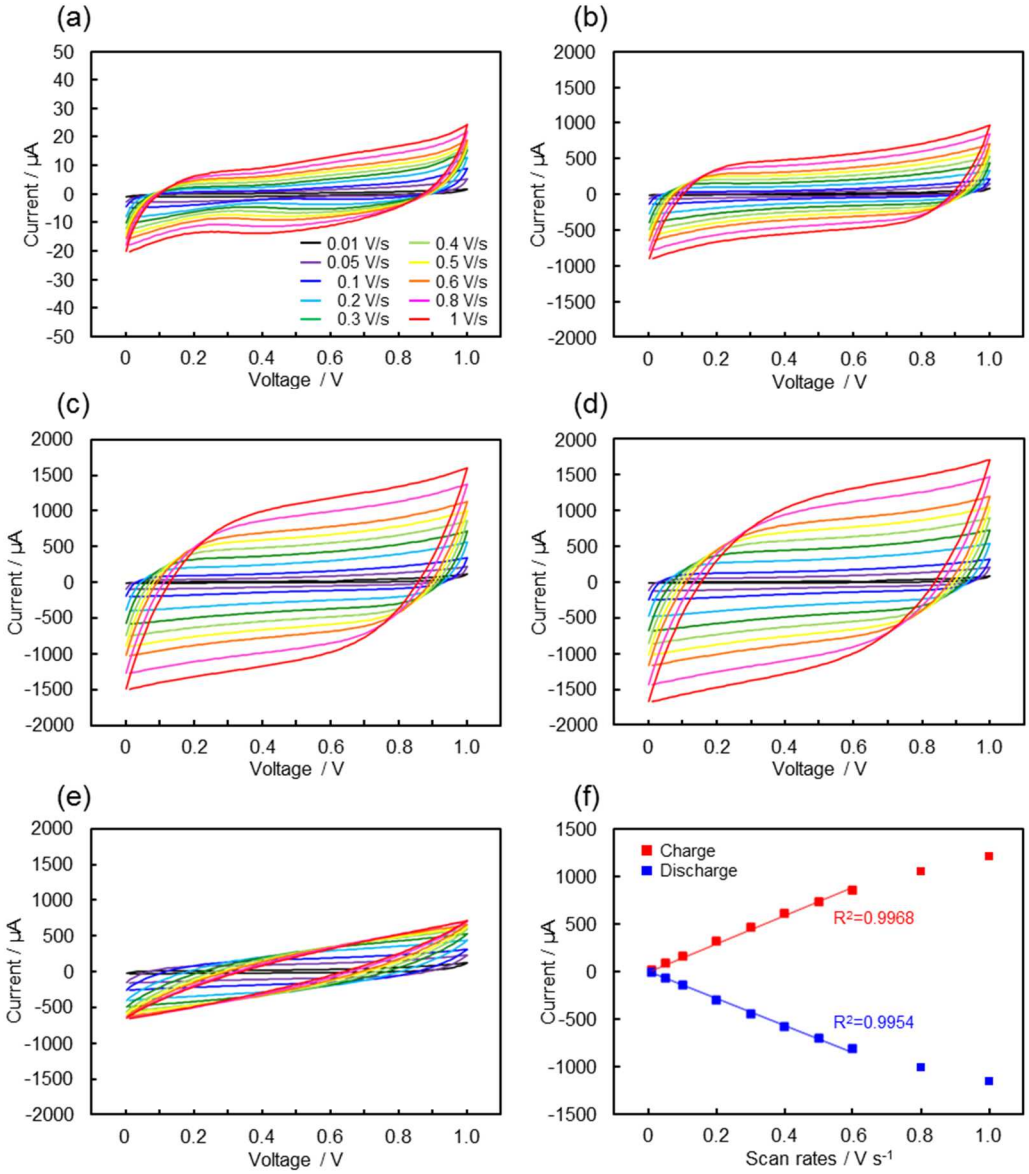

Figure 3-5. CV profiles of GOSC at various scan rates, where the GOSC samples were prepared using various photoreduction times: (a) Before photoreduction, (b) GOSC-1 h, (c) GOSC-3 h, (d) GOSC-6 h and (d) GOSC-12 h. (f) Dependence of the capacitive current (extracted from the CV profiles at 0.5 V) of GOSC-6 h in the applied scan rate between 10 to 1,000 mV s^{-1}. A linear relationship is observed with R^2 = 0.9968 and 0.9954 for the charge and discharge curves at least up to 600 mV s^{-1}, respectively. In contrast to our GOSC-6 h, GO-based micro-supercapacitor exhibits the desired rectangular CV shape only at slow scan rates, 2 to 200 mV s^{-1},[10,17] indicating the limited rate performance of this supercapacitor.

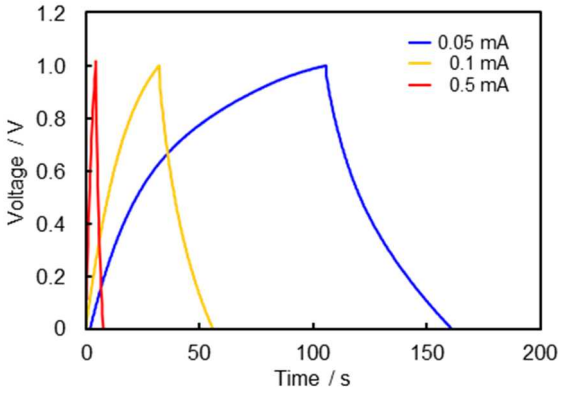

Figure 3-6. Galvanostatic charge/discharge curves of GOSC-6 h collected at different current densities. The specific capacitances of the samples were 2.1 (0.05 mA), 1.7 (0.1 mA) and 1.3 mF cm^{-2} (0.5 mA).

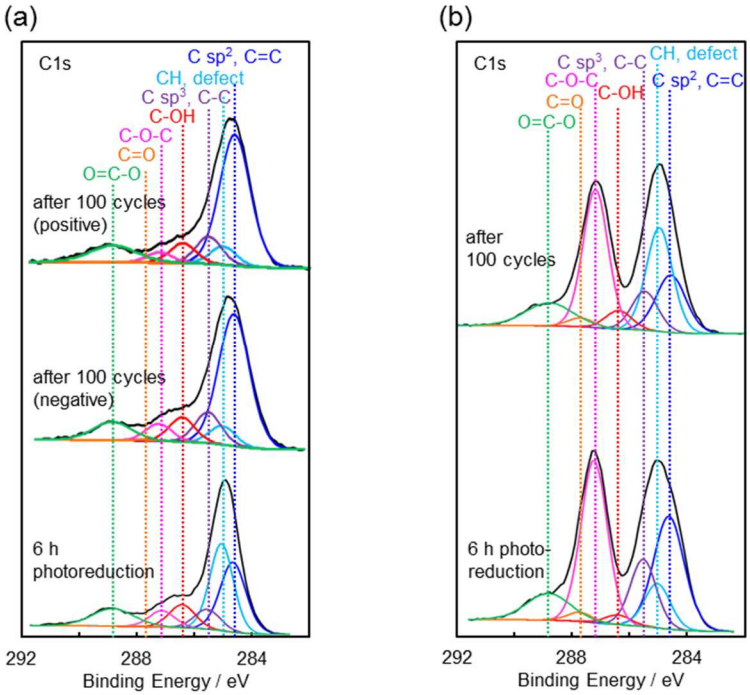

Figure 3-7. C 1s XPS spectra of (a) rGO electrode and (b) GO interlayer of GOSC-6 h before and after charge/discharge cycles. The interlayer of GOSC-6 h was obtained by peeling off the rGO layer using scotch tape.

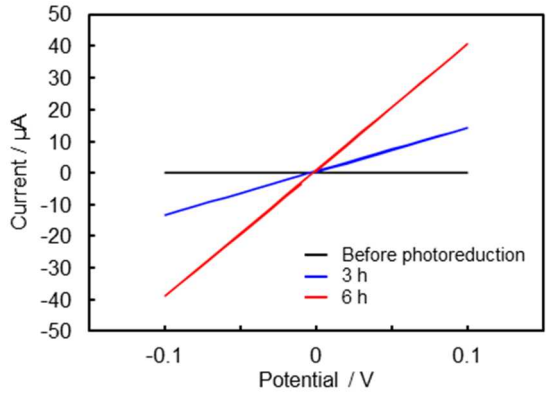

Figure 3-8. Typical *I–V* curves of GO and rGO films prepared at various photoreduction times. The electron conductivities were 2.04×10^{-9} (before photoreduction), 1.41×10^{-2} (3 h) and 4.03×10^{-2} S cm^{-1} (6 h).

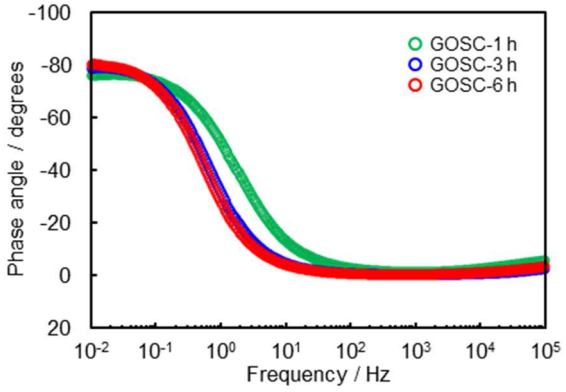

Figure 3-9. Impedance phase angle versus frequency for GOSC prepared using various photoreduction times. The corresponding time constant (τ_0) was calculated from $\tau_0 = 1/f_0$ (f_0: phase angle of −45°)

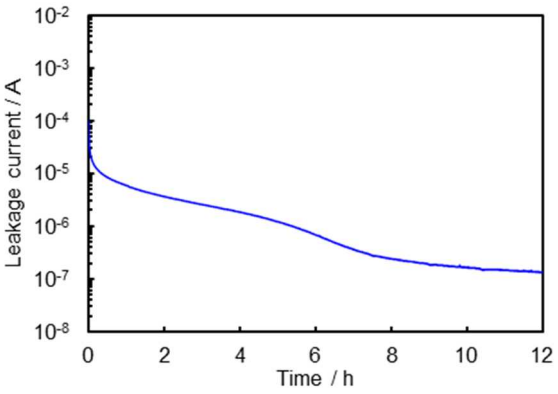

Figure 3-10. Leakage current measurement of GOSC-6 h. A DC voltage (the voltage at which the supercapacitor was operated, V_{max} = 1.0 V) was applied across the GOSC-6 h device; the current required to retain this voltage was measured over a period of 12 h.

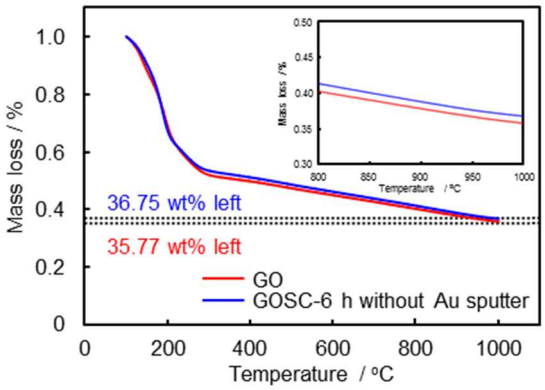

Figure 3-11. TGA plots of GO and GOSC-6 h without Au sputter. The mass of rGO active material for one electrode was calculated to be approximately 0.4 wt% of the total mass of GOSC-6 h without Au sputter (Details on calculation are given below in in Experimental section 3.2.6.2). However, the mass of the rGO active material is very small, as in the case of other micro-devices.[10,17,18] Therefore, we summarised the specific capacitance of GOSC based on the area of the rGO electrode.

Table 3-1. Summary of GOSC performance.

		Current (mA)	Capacitance (mF cm^{-2})	Capacitance (mF cm^{-3})	Power density (W cm^{-3})	Energy density (Wh cm^{-3})
GOSC-0 h	CV	-	0.01	-	-	-
	CC	0.05	0.07	0.03	0.02	2.63×10^{-6}
		0.1	0.06	0.02	0.01	1.79×10^{-6}
		0.5	-	-	-	-
GOSC-1 h	CV	-	0.39	-	-	-
	CC	0.05	0.44	0.18	0.06	2.09×10^{-5}
		0.1	0.35	0.14	0.04	1.35×10^{-5}
		0.5	-	-	-	-
GOSC-3 h	CV	-	0.83	-	-	-
	CC	0.05	0.82	0.33	0.13	4.25×10^{-5}
		0.1	0.69	0.28	0.13	3.38×10^{-5}
		0.5	0.56	0.23	0.09	1.64×10^{-5}
GOSC-6 h	CV	-	1.00	-	-	-
	CC	0.05	2.07	0.83	0.12	1.06×10^{-4}
		0.1	1.74	0.70	0.13	8.47×10^{-5}
		0.5	1.30	0.52	0.13	4.38×10^{-5}

Note: The volumetric stack capacitance (F cm^{-3}) of GOSC was calculated with the volume of the device taken into account, including the rGO, GO and Au current collector.

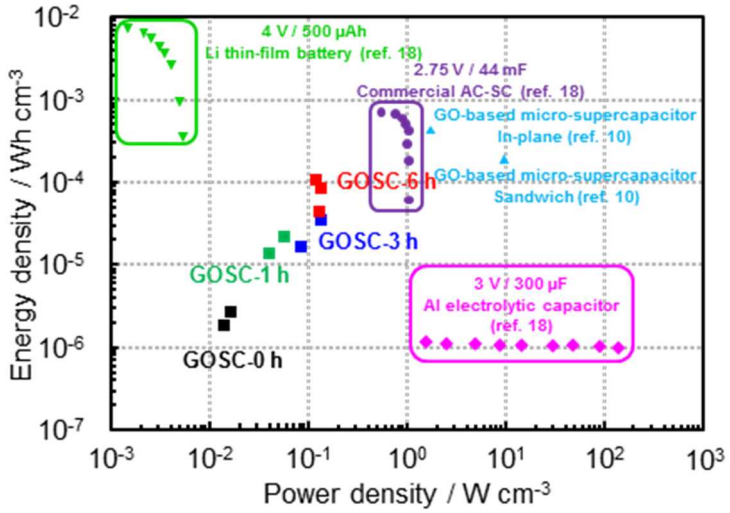

Figure 3-12. Comparative Ragone plot of a Li thin film battery,[18] commercial supercapacitor,[18] Al electrolytic capacitor,[18] GO-based micro-supercapacitor[10] and GOSC.

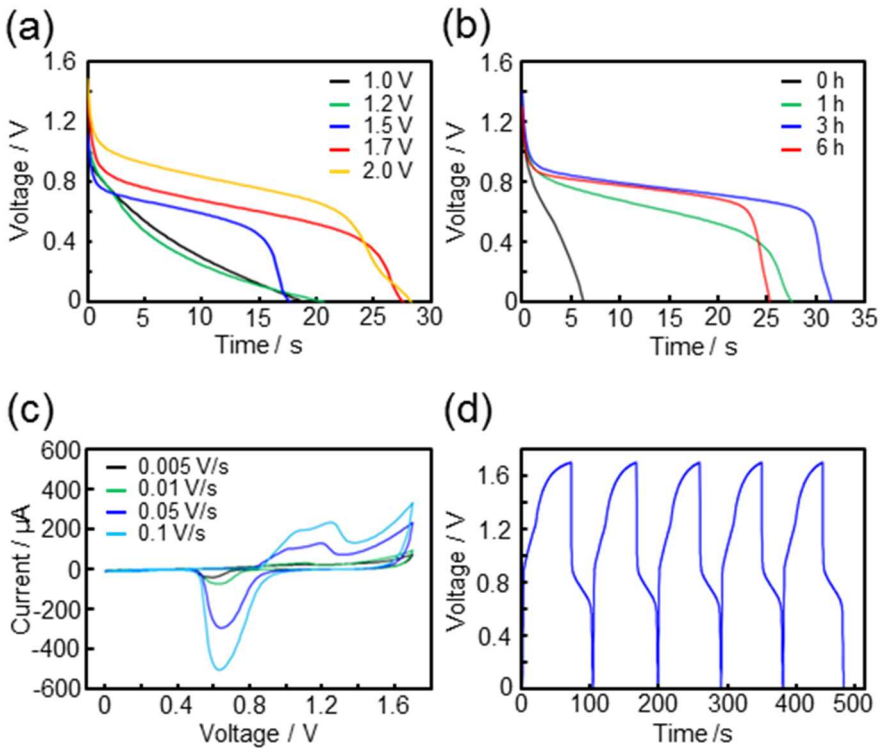

Figure 3-13. (a) Discharge profiles of GORB-1 h charged to various voltages at 0.05 mA. (b) Discharge profiles of GORB prepared with various photoreduction times at 0.05 mA. (c) CV profiles of GORB-3 h at various scan rates. (d) CC of GOSC-3 h at 0.05 mA.

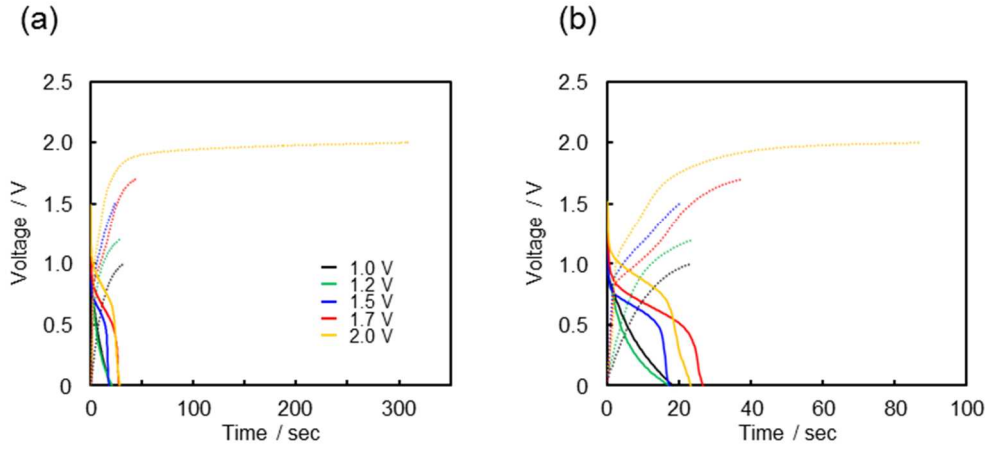

Figure 3-14. Galvanostatic charge/discharge curves of the rGO/GO/rGO device charged to various voltages at a current density of 0.05 mA cm^{-2}: (a) 1st cycle and (b) 5th cycle.

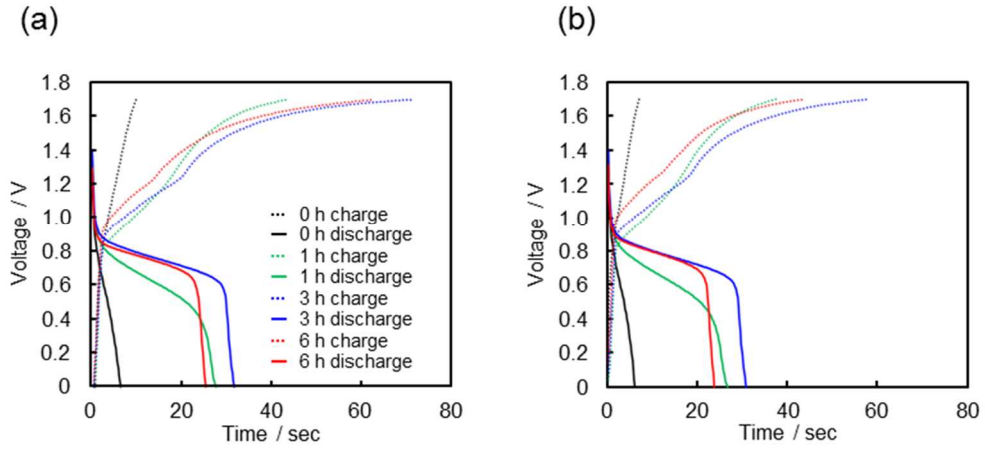

Figure 3-15. Galvanostatic charge/discharge curves of GORB prepared using various photoreduction times at a current density of 0.05 mA cm^{-2}: (a) 1st cycle and (b) 5th cycle.

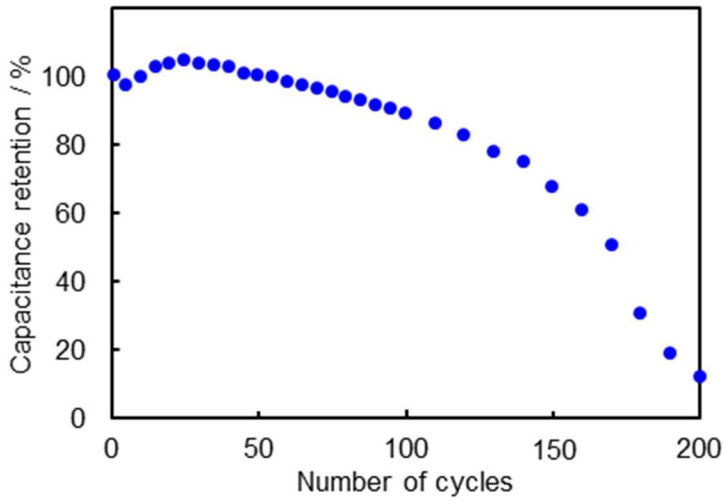

Figure 3-16. Cycle stability of GORB-3 h at 0.05 mA. Capacitance degradation was observed in GORB-3 h after 200 charge/discharge cycles. According to XPS analysis (Figure 3-17), decreases in the oxygenated functional groups and increases in the CH defects of rGO anode were observed after 200 charge/discharge cycles. On the other hand, XPS spectra of the rGO cathode were barely changed. Thus, in the case of our GORB, we speculate that the main reasons of capacitance degradation were (1) decreasing the redox site of the rGO anode and (2) decreasing electron conductivity of the rGO anode derived increasing from CH defects.

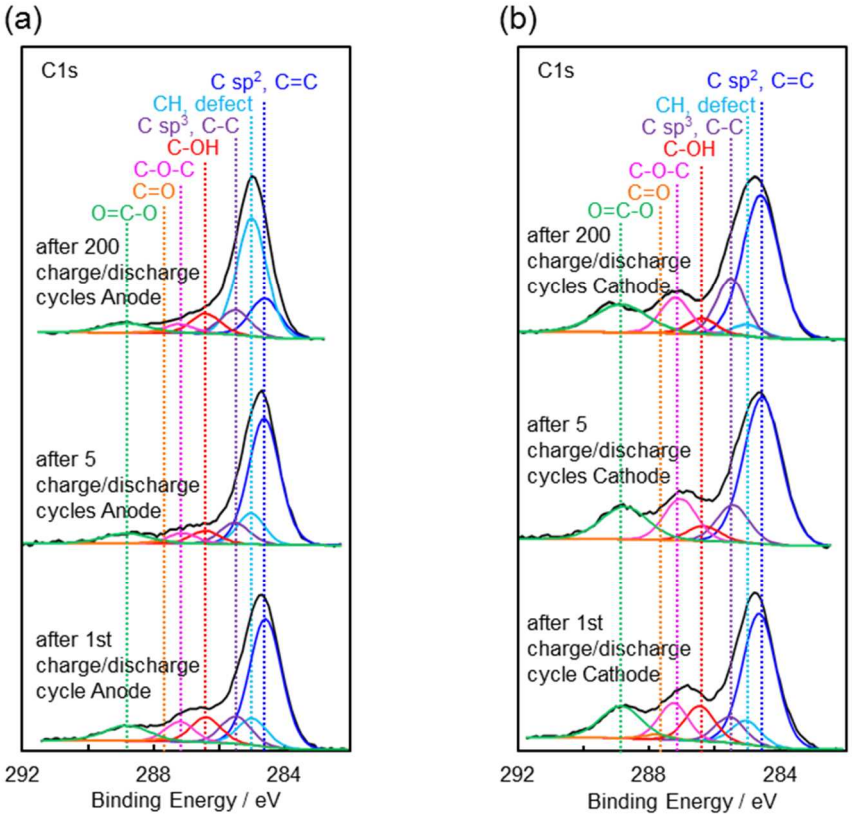

Figure 3-17. C 1s XPS spectra of (a) anode and (b) cathode of GORB-3 h after various charge/discharge cycles.

References

(1) J. A. Turner, *Science*, 1999, **285**, 687-689.

(2) (a) K. Kang, Y. S. Meng, J. Breger, C. P. Grey, and G. Ceder, *Science*, 2006, **311**, 977-980; (b) F. Bonaccorso, L. Colombo, G. Yu, M. Stoller, V. Tozzini, A. C. Ferrari, R. S. Ruoff, and V. Pellegrini, *Science*, 2015, **347**, 6217.

(3) (a) M. D. Stoller, S. Park, Y. Zhu, J. An, and R. S. Ruoff, *Nano Lett.*, 2008, **8**, 3498-3502; (b) G. Xiong, C. Meng, R. G. Reifenberger, P. P. Irazoqui, and T. S. Fisher, *Electroanalysis*, 2014, **26**, 30-51.

(4) B. Dunn, H. Kamath, and J. M. Tarascon, *Science*, 2011, **334**, 928-935.

(5) (a) Y. Gogotsi and P. Simon, *Science*, 2011, **334**, 917-918; (b) M. F. El-Kady, V. Strong, S. Dubin, and R. B. Kaner, *Science*, 2012, **335**, 1326-1330.

(6) P. Simon, Y. Gogotsi, and B. Dunn, *Science*, 2014, **343**, 1210-1211.

(7) R. R. Nair, H. A. Wu, P. N. Jayaram, I. V. Grigorieva, and A. K. Geim, *Science*, 2012, **335**, 442-444.

(8) (a) H. W. Kim, H. W. Yoon, S. M. Yoon, B. M. Yoo, B. K. Ahn, Y. H. Cho, H. J. Shin, H. Yang, U. Paik, S. Kwon, J. Y. Choi, and H. B. Park, *Science*, 2013, **342**, 91-95; (b) P. Sun, F. Zheng, M. Zhu, Z. Song, K. Wang, M. Zhong, D. Wu, R. B. Little, Z. Xu, and H. Zhu, *ACS Nano*, 2014, **8**, 850-859.

(9) (a) M. R. Karim, K. Hatakeyama, T. Matsui, H. Takehira, T. Taniguchi, M. Koinuma, Y. Matsumoto, T. Akutagawa, T. Nakamura, S. Noro, T. Yamada, H. Kitagawa, and S. Hayami, *J. Am. Chem. Soc*., 2013, **135**, 8097-8100; (b) K. Hatakeyama, M. R. Karim, C. Ogata, H. Tateishi, A. Funatsu, T. Taniguchi, M. Koinuma, S. Hayami, and Y. Matsumoto, *Angew. Chem. Int. Ed*., 2014, **53**, 6997-7000.

(10) W. Gao, N. Singh, L. Song, Z. Liu, A. L. M. Reddy, L. Ci, R. Vajtai, Q. Zhang, B. Wei, and P. M. Ajayan, *Nat. Nanotechnol*., 2011, **6**, 496-500.

(11) (a) X. Yang, F. Zhang, L. Zhang, T. Zhang, Y. Huang, and Y. Chen, *Adv. Funct. Mater.*, 2013, **23**, 3353-3360; (b) X. Yang, L. Zhang, F. Zhang, T. Zhang, Y. Huang, and Y. Chen, *Carbon*, 2014, **72**, 381-386.

(12) (a) Ravikumar and K. Scott, *Chem. Commun.*, 2012, **48**, 5584-5586; (b) H. Tateishi, K. Hatakeyama, C. Ogata, K. Gezuhara, J. Kuroda, A. Funatsu, M. Koinuma, T. Taniguchi, S. Hayami, and Y. Matsumoto, *J. Electrochem. Soc.*, 2013, **160**, F1175-F1178.

(13) H. Tateishi, T. Koga, K. Hatakeyama, A. Funatsu, M. Koinuma, T. Taniguchi, and Y. Matsumoto, *ECS Electrochem. Lett.*, 2014, **3**, A19-A21.

(14) J. Q. Huang, T. Z. Zhuang, Q. Zhang, H. J. Peng, C. M. Chen, and F. Wei, *ACS Nano*, 2015, **9**, 3002-3011.

(15) H. Kim, K. Y. Park, J. Hong, and K. Kang, *Sci. Rep*., 2014, **4**, 5278.

(16) W. S. Hummers, and R. E. Offeman, *J. Am. Chem. Soc.*, 1958, **80**, 1339.

(17) Q. Zhang, K. Scrafford, M. Li, Z. Cao, Z. Xia, P. M. Ajayan, and B. Wei, *Nano Lett.*, 2014, **14**, 1938-1943.

(18) M. F. El-Kady and R. B. Kaner, *Nat. Commun.*, 2013, **4**, 1475.

(19) (a) H. Tateishi, M. Koinuma, S. Miyamoto, Y. Kamei, K. Hatakeyama, C. Ogata, T. Taniguchi, A. Funatsu, and Y. Matsumoto, *Carbon*, 2014, **76**, 40-45; (b) J. Lin, Z. Peng, Y. Liu, F. Ruiz-Zepeda, R. Ye, E. L. G. Samuel, M. J. Yacaman, B. I. Yakobson, and J. M. Tour, *Nat. Commun*., 2014, **5**, 5714.

(20) K. Kobayashi, M. Nagao, Y. Yamamoto, P. Heo, and T. Hibino, *J. Electrochem. Soc.*, 2015, **162**, F868-F877.

(21) T. Tomai, S. Mitani, D. Komatsu, Y. Kawaguchi, and I. Honma, *Sci. Rep.*, 2014, **4**, 3591.

(22) (a) X. Fan, Y. Lu, H. Xu, X. Kong, and J. Wang, *J. Mater. Chem.*, 2011, **21**, 18753-18760; (b) C. M. Chen, Q. Zhang, M. G. Yang, C. H. Huang, Y. G. Yang, and M. Z. Wang, *Carbon*, 2012, **50**,

3572-3584; (c) A. Y. S. Eng, A. Ambrosi, C. K. Chua, F. Sanek, Z. Sofer, and M. Pumera, *Chem. Eur. J.*, 2013, **19**, 12673-12683; (d) G. D. O'Neil, A. W. Weber, R. Buiculescu, N. A. Chaniotakis, and S. P. Kounaves, *Langmuir*, 2014, **30**, 9599−9606; (e) J. Li, C. Chen, J. Wei, J. Li, and X. Wang, *J. Phys. Chem. C*, 2014, **118**, 28440-28447.

(23) (a) B. Huskinson, M. P. Marshak, C. Suh, S. Er, M. R. Gerhardt, C. J. Galvin, X. Chen, A. Aspuru-Guzik, R. G. Gordon, and M. J. Aziz, *Nature*, 2014, **505**, 195-198; (b) S. Er, C. Suh, M. P. Marshaka, and A. Aspuru-Guzik, *Chem. Sci.*, 2015, **6**, 885-893.

CHAPTER 4

General Conclusion

As hydrated GO is simultaneously a good ionic conductor and an electrical insulator, GO can be used as both a separator and electrolyte. Moreover, rGO is suitable for electrode materials owing to its high electrical conductivity and high specific surface area. Based on these considerations, the rGO/GO/rGO structure, which is composed of a GO electrolyte/separator and rGO electrodes, is expected to perform as an electrical device. In this work, we investigated the (1) functionalities of the interlayer nanospace in multilayered GO and (2) the electrochemical properties of an all-carbon SC (Graphene Oxide Supercapacitor: GOSC) and redox battery (Graphene Oxide Redox Battery: GORB).

A summary of each chapter is given below.

- **Chapter 1** detailed the general background of graphene-based materials, energy storage devices, and aim of the present study.
- **Chapter 2** demonstrated the new functionalities of the interlayer nanospace in multi-layered GO for ion diffusion and reaction at the metal/GO (M/GO) interface. Understanding the chemical and physical properties of M/GO interfaces is important when GO is used in electronic and electrochemical devices because the metal layer must be firmly attached to the GO. Permeation of metal from the surface into GO paper bulk at the M/GO interface was observed at room temperature for metals such as Cu, Ag, Ni, Au, and Pt. Cu, Ag, and Ni quickly permeated through GO as ions into the bulk under humid conditions. At first, these metals changed to hydrated ions as a result of redox reactions (with reduction of GO) at the surface, and then permeated the interlayers. Au and Pt were observed to permeate GO into the GO bulk at room temperature as atoms, although the permeation rates were low. These surprising results are considered to be due to the presence of many

defects and/or edges with oxygenated groups in the GO paper. The interlayer nanospace in multilayered GO presents two types of layers: (1) π–π hydrophobic interaction layers based on the graphene domain and (2) hydrophilic interaction layers derived from the oxygen functional group. Therefore, the redox reaction of the M/GO interface and ion diffusion behavior based on this unique interlayer nanospace in the GO membrane must be an important aspect of the development of solid GO electrolytes including metal ions for the electrochemical device.

- **Chapter 3** presented the development of new all-carbon electrochemical devices—GOSC and GORB. This device with rGO/GO/rGO structure was easily fabricated *via* photo irradiation of both surfaces of a GO film in a single step. Moreover, this device functioned as both a SC and battery depending on the working voltage. The rGO/GO/rGO device operated as a proton-type SC at working potentials as high as 1.2 V. The GOSC exhibited high specific area capacitance of 2 mF cm^{-2} even when operated at high scan rates of 1,000 mV s^{-1}. We speculate that the charge storage mechanism of GOSC resulted from (1) proton conductivity and (2) polarized/separated water molecules in the interlayer spacing of the nanoscale GO. At potentials greater than 1.5 V, it behaved as a battery that operated on the basis of the redox reactions between the oxygenated functional groups on the rGO. In particular, the GORB, which had a plateau potential of approximately 0.75 V and coulombic efficiency of approximately 53%, exhibited excellent battery behavior at a charge voltage of 1.7 V. The rGO/GO/rGO device, which comprises two different rGO electrodes with redox couples based on two different functional groups with dissimilar reaction potentials, functioned as a battery. We deduced the following two hypotheses for the redox mechanism of the GORB: (1) cathode: $C{=}O + H^+ + e^- \leftrightarrow C{-}OH$; anode: CH (defect) + $CO_2 \leftrightarrow$ 2C=O (or C–O) + $H^+ + e^-$; or (2) cathode: $4H^+ + 4e^- + O_2 \leftrightarrow H_2O$; anode: CH (defect) + $CO_2 \leftrightarrow$ 2C=O (or C–O) + $H^+ + e^-$. From a practical viewpoint, the performance of the GOSC and GORB should be further improved. Nonetheless, our research demonstrates possibilities for a GOSC/GORB

to be advanced energy storage devices that can be operated at low temperature and low humidity. This work, as a solution to bridge the gap between batteries and SCs, sheds new light on the development of energy storage devices.

- **Chapter 4** gave the general conclusion of the thesis. In this work, we demonstrated **(1) new functionalities of the interlayer nanospace in multilayered GO for ion diffusion and reaction of the M/GO interface**, and we succeeded in synthesizing and operating **(2) new all-carbon electrochemical devices—Graphene Oxide Supercapacitor (GOSC) and Graphene Oxide Redox Battery (GORB)—with tunable SC and battery behavior *via* the working voltage for the first time to our knowledge.** The redox reaction of the M/GO interface and ion diffusion behavior based on the unique interlayer nanospace in the GO membrane must be an important aspect of the development of solid GO electrolytes including metal ions for the electrochemical devices. Moreover, we believe that all-carbon electrochemical devices, which function as both a SC and battery, are attractive and will evolve as next generation electrochemical devices.

ACKNOWLEDGEMENTS

I would like to express my most sincere thanks to **Professor Yasumichi Matsumoto** for his invaluable comments and suggestions in addition to his encouragement through the period of this study.

I would also like to thank the other members of my committee: Professor Seiji Kurihara, Professor Masato Machida, Associate Professor Michio Koinuma, and Professor Shinya Hayami.

I would like to express my appreciation to Assistant Professor Takaaki Taniguchi and Associate Professor Shintaro Ida for their advice and encouragement.

I would like to express my deepest appreciation to Assistant Professor Asami Funatsu and Associate Professor Masayo Sakata for their advice, teachings, and encouragement during my academic tenure.

I would like to express my deepest appreciation to Ms. Kiyomi Tahara (secretary) and Ms. Tomoko Tsuchiyama (secretary) in this laboratory for their advice and assistance.

I am deeply thankful to Dr. Kazuto Hatakeyama, Dr. Hikaru Tateishi, Mr. Yusuke Watanabe, Mr. Kengo Gezuhara, Mr. Jun Kuroda, and Ms. Ruriko Kurogi for their encouragement and assistance.

I am also thankful to the students in the Koinuma Laboratory.

Finally, I deeply thank my parents, husband, daughter, and older sister for their support and hearty encouragement throughout my tenure as a graduate student.

Chikako Ueda

Kumamoto

2016